ABSTRACT

EFFECT OF POLYMORPHIC PHASE TRANSFORMATIONS WITHIN AN ALUMINA LAYER ON THE IGNITION OF ALUMINUM PARTICLES

by
Mikhaylo Aleksiyovych Trunov

Experimental measurements of aluminum ignition temperature and models used to describe aluminum ignition are reviewed. It is shown that the current models cannot describe ignition of aluminum powders of different sizes and ignited under various experimental conditions. The properties of and phase changes occurring in the alumina scale existing on the surface of aluminum particles at different temperatures are systematically studied. The mechanism of aluminum oxidation is quantified and a new simplified ignition model is developed.

Thermogravimetry was used to study the oxidation of aluminum powders of various particle sizes and surface morphologies in oxygen at temperatures up to 1500 °C. Partially oxidized samples were recovered from selected intermediate temperatures and the oxide phases present were analyzed by x-ray diffraction. Both micron- and nano-sized aluminum powders were observed to exhibit characteristic stagewise oxidation in the temperature range from 300 to 1500 °C. Kinetic parameters for both direct oxidative growth of alumina scale and phase transformations between different alumina polymorphs were determined from the thermal analysis data for a selected micron-sized powder. The observed oxidation trends for other micron- and nano-sized powders were well interpreted considering the established kinetics.

Melting of aluminum nanopowders was studied by differential scanning calorimetry in argon environment. No correlation was found between the melting and oxidation.

The developed aluminum ignition model describes ignition of a particle inserted in a hot oxygenated gas environment – scenario similar to the particle ignition in a reflected shock in a shock tube experiment. The model treats heterogeneous oxidation as an exothermic process leading to ignition. The ignition is assumed to occur when the particle's temperature exceeds the alumina melting point. The model analyzes processes of simultaneous growth and phase transformations in the oxide scale. Additional assumptions about oxidation rates are made to account for discontinuities produced in the oxide scale as a result of increase in its density caused by the polymorphic phase changes. The model predicts that particles of different sizes ignite at different environment temperatures. Generally, finer particles ignite at lower temperatures. The model consistently interprets a wide range of the previously published experimental data describing aluminum ignition.

EFFECT OF POLYMORPHIC PHASE TRANSFORMATIONS WITHIN AN ALUMINA LAYER ON THE IGNITION OF ALUMINUM PARTICLES

by
Mikhaylo Aleksiyovych Trunov

A Dissertation
Submitted to the Faculty of
New Jersey Institute of Technology
in Partial Fulfillment of the Requirements for the Degree of
Doctor of Philosophy in Mechanical Engineering

Department of Mechanical Engineering

May 2006

APPROVAL PAGE

EFFECT OF POLYMORPHIC PHASE TRANSFORMATIONS WITHIN AN ALUMINA LAYER ON THE IGNITION OF ALUMINUM PARTICLES

Mikhaylo Aleksiyovych Trunov

Dr. Edward L. Dreizin, Dissertation Advisor — Date
Professor of Mechanical Engineering, NJIT

Dr. Rajesh N. Dave, Committee Member — Date
Professor of Mechanical Engineering, NJIT

Dr. Nick G. Glumac, Committee Member — Date
Associate Professor of Mechanical and Industrial Engineering,
University of Illinois at Urbana-Champaign

Dr. Boris Khusid, Committee Member — Date
Professor of Mechanical Engineering, NJIT

Dr. Mirko Schoenitz, Committee Member — Date
Research Assistant Professor of Mechanical Engineering, NJIT

BIOGRAPHICAL SKETCH

Author: Mikhaylo Aleksiyovych Trunov

Degree: Doctor of Philosophy

Date: May 2006

Undergraduate and Graduate Education:

- Doctor of Philosophy in Mechanical Engineering,
  New Jersey Institute of Technology, Newark, NJ, 2006

- Master of Science in Physics,
  Odessa University, Odessa, Ukraine, 1985

Major: Mechanical Engineering

Presentations and Publications:

Mikhaylo A. Trunov, Swati M. Umbrajkar, Mirko Schoenitz, Joseph T. Mang, and Edward L. Dreizin,
"Oxidation and Melting of Aluminum Nanopowders,"
Journal of Physical Chemistry B, [submitted] 2006.

Mikhaylo A. Trunov, Mirko Schoenitz, and Edward L. Dreizin,
"Effect of Polymorphic Phase Transformations in Alumina Layer on Ignition of Aluminum Particles,"
Combustion Theory and Modeling, [in print] 2006.

Yuriy L. Shoshin, Mikhaylo A. Trunov, Xiaoying Zhu, Mirko Schoenitz, and Edward L. Dreizin,
"Ignition of Aluminum-Rich Al-Ti Mechanical Alloys in Air,"
Combustion and Flame, 144, pp. 688-697, 2006.

Mikhaylo A. Trunov, Mirko Schoenitz, Xiaoying Zhu, and Edward L. Dreizin,
"Effect of Polymorphic Phase Transformations in Al_2O_3 Film on Oxidation Kinetics of Aluminum Powders,"
Combustion and Flame, 140, pp. 310-318, 2005.

Mikhaylo A. Trunov, Mirko Schoenitz, and Edward L. Dreizin,
"Ignition of Aluminum Powders under Different Experimental Conditions,"
Propellants, Explosives, Pyrotechnics, 30 (1), pp. 36-43, 2005.

Trent S. Ward, Mikhaylo A. Trunov, Mirko Schoenitz, and Edward L. Dreizin,
"Experimental Methodology and Heat Transfer Model for Identification of Ignition Kinetics of Powdered Fuels,"
International Journal of Heat and Mass Transfer, [submitted] 2005.

Swati M. Umbrajkar, Mikhaylo A. Trunov, Mirko Schoenitz, and Edward L. Dreizin,
"Melting and Oxidation of Nanometer Size Aluminum Powders,"
Proceedings of 2005 MRS Fall Meeting, Boston, MA, November 28 – December 2, [in print] 2005.

Trent S. Ward, Mikhaylo A. Trunov, and Edward L. Dreizin,
"Heat Transfer Model for Ignition of Metal Powder on a Heated Filament,"
4th Joint Meeting of the US Section of the Combustion Institute, Philadelphia, PA, proceedings published on CD-ROM by Omnipress, 2005.

Mikhaylo A. Trunov, Mirko Schoenitz, and Edward L. Dreizin,
"Effect of Polymorphic Phase Transformations in Alumina Layer on Ignition of Aluminum Particles,"
4th Joint Meeting of the US Section of the Combustion Institute, Philadelphia, PA, proceedings published on CD-ROM by Omnipress, 2005.

Mikhaylo A. Trunov, Mirko Schoenitz, and Edward L. Dreizin,
"Ignition of Al-Mg Mechanical Alloys,"
In: Novel Energetic Materials and Application, Edited Book of Proceedings of the Ninth International Workshop on Combustion and Propulsion (Eds: DeLuca L., Galfetti L., Pesce-Rodriguez R.A.), Arzago d'Adda, BG, Italy, pp. 9.1 – 9.13, 2004.

Mikhaylo A. Trunov, and Edward L. Dreizin,
"Ignition of Metastable Metal Based High Energy Density Fuels,"
The 9th International Workshop on Combustion and Propulsion, Lerici, La Spezia, Italy, pp. 36-40, September 2003.

Salil Mohan, Mikhaylo A. Trunov, and Edward L. Dreizin,
"Characterization of Aluminum Powder Ignition,"
The 2003 Technical Meeting of the Eastern States Section of the Combustion Institute, State College, PA, pp. 329-332, October 2003.

Mikhaylo A. Trunov, Mirko Schoenitz, and Edward L. Dreizin,
"Ignition of Al-Mg Mechanical Alloys,"
The 2003 Technical Meeting of the Eastern States Section of the Combustion Institute, State College, PA, pp. 313-316, October 2003.

To my parents

ACKNOWLEDGMENT

I would like to express my appreciation to Professor Dreizin who served as a dissertation adviser, and has been a life long friend. I am grateful to my co-authors: Xiaoying Zhu and Swati M. Umbrajkar whose help with experiments was invaluable. I acknowledge all the help from Dr. Mirko Schoenitz who is not only served as my committee member, but also has been a thoughtful colleague and co-author. I would like to thank Dr. Joseph T. Mang for measuring particle size distributions of aluminum nano powders. Special thanks are given to Drs. Rajesh N. Dave, Nick G. Glumac, and Boris Khusid for active participation in my committee.

TABLE OF CONTENTS

TABLE OF CONTENTS
(Continued)

TABLE OF CONTENTS
(Continued)

Chapter **Page**

LIST OF TABLES

LIST OF FIGURES

LIST OF FIGURES
(Continued)

LIST OF SYMBOLS

A	reaction controlled species
B	pre-exponent
C	concentration
c	heat capacity
$C_{oxidizer}$	concentration of oxidizer
C_A	concentration of reaction controlled species
C_A^*	combined oxidation constant
C_A^{Al}	concentration of reaction controlled species on oxide-aluminum interface
C_A^{ox}	concentration of reaction controlled species on oxide-gas interface
C_i	pre-exponent describing diffusion within alumina polymorph specified by the subscript
C_i^e	effective value of pre-exponent describing diffusion within alumina polymorph specified by the subscript
D	initial diameter of aluminum core
D_A	diffusion coefficient of reaction controlled species
$\langle D \rangle_k$	geometric mean diameters
D_{O_2}	coefficient of oxygen diffusion in air
d	diameter
d_{BET}	diameter determined by the Brunauer-Emmett-Teller method
E	activation energy
E_i	activation energy of growth of alumina polymorph specified by the subscript
$E_{(i-1)\to i}$	activation energy of polymorphic transformation between alumina polymorphs specified by the subscript
$F_{(i-1)\to i}$	pre-exponent describing rate of polymorphic transformation between alumina polymorphs specified by the subscript
f	fraction of open aluminum surface
G_i	empirical parameter describing alumina polymorph specified by the subscript

H_b entalphy of bulk aluminum fusion

H_m latent heat of nanoparticle melting

H_{oxi} entalphy of oxidation

h thickness

h_i thickness of alumina polymorph specified by the subscript

$h_i^{'}$ initial thickness of alumina polymorph specified by the subscript

h_i^e minimum thickness of a growing alumina layer specified by the subscript at which its diffusion resistance becomes that of a regular polycrystalline film

h_i^m minimum thickness of a growing alumina layer specified by the subscript at which its diffusion resistance becomes non-negligible

$K_{(i-1)\to i}$ empirical parameter describing phase transformation between alumina polymorphs specified by the subscript

L_i empirical coefficient describing alumina polymorph specified by the subscript

l length of atomic bond

M_s parameter accounting for frequency function normalization and proportional to the mass of aluminum in a sample

m sample mass

$\dot{m}$ rate of sample mass change

$\dot{m}^{ox}$ rate of mass change due to direct aluminum oxidation

$\dot{m}_i^{ox}$ rate of mass change due to direct aluminum oxidation limited by diffusion through alumina polymorph specified by the subscript

$\dot{m}_{\gamma,O_2}^{ox}$ rate of aluminum oxidation during gamma alumina polymorph formation that is limited by gas phase diffusion of oxygen

$\dot{m}^{tr}$ rate of polymorphic phase transformations

$\dot{m}_{(i-1)\to i}^{tr}$ rate of polymorphic phase transformations between alumina polymorphs specified by the subscript

m_N normalized sample mass

$\hat{m}_S$ experimental sample mass

$\hat{m}_S'$ initial experimental sample mass

N_A diffusion molar rate

Nu	the Nusselt number
P	frequency function
$\dot{Q}$	heat transfer rate
$\dot{Q}_{DSC}$	modeled differential scanning calorimetry signal
R	the universal gas constant
r	radius
r_i	radius of a phase specified by the subscript
r_i'	initial radius of a phase specified by the subscript
S	surface
S_{BET}	specific surface determined by the Brunauer-Emmett-Teller method
T	temperature
T_b	melting point of bulk aluminum
T_m	melting point
t	time
V	volume
$\dot{V}$	rate of volume change
$\dot{V}_i$	rate of volume change of a phase specified by the subscript
$\dot{V}_i^{rel}$	rate of relative volume change of a phase specified by the subscript
V_i'	initial volume of a phase specified by the subscript
W	weight factor
X_i	empirical parameter describing alumina polymorph specified by the subscript
α	alpha phase of alumina
β	heating rate
χ	molar fraction of oxygen in a gaseous environment
Δm	mass change
δ	delta phase of alumina
ε	emissivity
γ	gamma phase of alumina

λ thermal conductivity

μ molar mass

$v_{(i-1)\rightarrow i}$ velocity of motion of interface between alumina polymorphs specified by the subscript

Θ diffraction angle

θ theta phase of alumina

ρ density

ρ_i density of a phase specified by the subscript

σ the Stefan-Boltzmann constant

σ_k geometric standard deviation

σ_{sl} surface tension on solid-liquid interface

subscripts

Al refer to aluminum

Al_2O_3 refer to aluminum oxide

am refer to amorphous alumina

ch refer to chemical reaction

e refer to environment

f refer to boundary layer

gas refer to gas environment

i refer to specific oxide polymorph

i-1 refer to underlying substrate

i-2 refer to underlying substrate

k refer to specific log-normal distribution

O_2 refer to oxygen

ox refer to alumina

p refer to particle

ph refer to physical heat transfer processes

α refer to alpha alumina

γ	refer to gamma alumina
∞	refer to surrounding surfaces

CHAPTER 1

REVIEW: IGNITION OF ALUMINUM POWDERS UNDER DIFFERENT EXPERIMENTAL CONDITIONS

1.1 Introduction

Aluminum powders are widely used as fuels in various energetic materials, including pyrotechnics, explosives, and propellants [1, 2]. The advantages of aluminized fuels are their high oxidation enthalpy, high combustion temperature, environmentally benign products, and relatively low cost. However, in many applications a long ignition delay of aluminum leads to agglomeration of molten particles (e.g., [3, 4]) and diminishes performance of the energetic formulation. Ignition and combustion of aluminum have been actively studied over the last 5 decades and a large body of experimental data was accumulated. This chapter reviews both experimental and theoretical studies of aluminum ignition. In addition, recent experimental results on aluminum oxidation are described and interpreted to outline qualitative mechanisms of ignition of aluminum powders in various experimental situations.

1.2 Experimental Studies of Aluminum Ignition

A large number of experimental investigations reported in the literature make it a formidable task to present a comprehensive review. Instead, several characteristic examples of experimental techniques used to determine the temperature of aluminum ignition are selected and described below.

1.2.1 Ignition of Aluminum Powder in a Flat Flame Burner

This technique developed by Friedman and Macek is described in Ref. [5]. A simplified schematic diagram of the experimental apparatus is shown in Fig. 1.1. A dilute fluidized bed containing aluminum powder was placed under a flat flame burner. The individual aluminum particles were fed into the post-flame region of the burned combustible gas mixture via a hypodermic needle. When individual aluminum particles entrained in combustion gases ignited, bright particle streaks were observed. The flame stoichiometry and gas flow rates were adjusted to determine the minimum gas temperature at which ignition occurred. The temperature of the combustion gases was calculated as an adiabatic flame temperature corrected by about 20 °C to account for heat losses to the water-cooled burner. The correction was supported by the measurements of the temperature rise in the cooling water and respective heat transfer calculation. Spherical 15 – 67 μm diameter aluminum powders were used in these experiments. The combustible gas mixtures were prepared using propane, oxygen, and nitrogen. The ignition was observed to occur when the gas temperature exceeded 1940 °C.

A flat flame burner was also used in more recent aluminum ignition studies, e.g., [6], where 45-53 μm diameter aluminum particles ignited in the combustion products of methane/oxygen/argon and methane/oxygen/nitrogen gas mixtures. The flat flame temperatures were measured from the absorption spectra of the OH radical. Particles were observed to ignite at about 1830 °C.

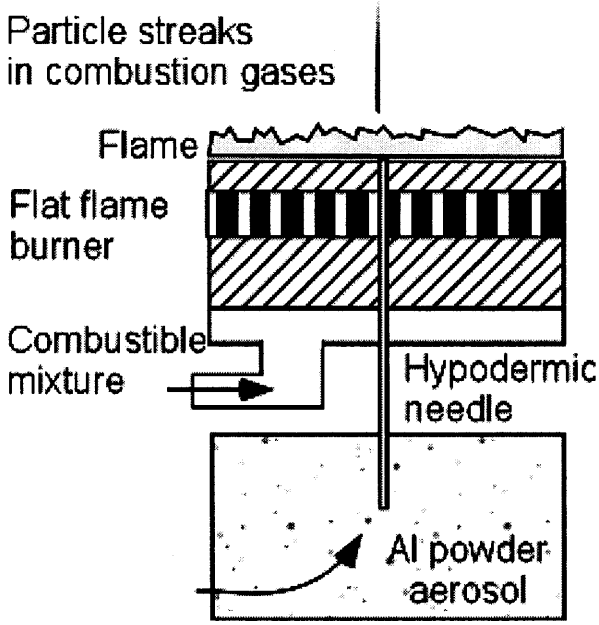

Figure 1.1 Schematic diagram of a flat flame burner experiment used in Ref. [5] to determine aluminum ignition temperature.

1.2.2 Ignition of Aluminum Wires

In these experiments, an electrically heated aluminum wire was placed in a flow of an oxidizing gas. The ignition temperature was determined optically, or from the measured changes in the wire resistance. Early experiments with this configuration were reported by Brzustowski and Glassman, [7] and Kuehl [8]. The technique was further developed by Merzhanov and co-workers [9] and used to determine ignition temperatures of aluminum wires in oxygen and carbon dioxide. A simplified diagram of the experimental setup used in Ref. [9] is shown in Fig. 1.2. The heated aluminum wire was placed within a rectangular tube and subjected to a controlled laminar gas flow. A dedicated power supply was designed to provide various regimes of heating the wire. The wire was heated with a constant power, a stepwise power increase, and an exponentially increasing power. The ignition temperature was determined from the wire resistance measured in real time.

Extensive heat transfer analyses and calibrations of the wire resistance as a function of temperature were used to support this measurement. For 30 - 50 μm diameter wires, ignition in pure oxygen occurred at 1640 – 2000 °C. These results are consistent with the data presented in Ref. [8]. The ignition temperature coinciding with the alumina melting point, 2053 °C was reported based on the optical pyrometry and similar experiments described in Ref. [7]. Analysis of the ignition temperature as a function of the heating rate was presented in Ref. [9]. The heating rates varied in vicinity of 10^2-10^3 °C/s. It was reported that higher ignition temperatures were observed at lower heating rates. The proposed interpretation suggested an increase in the ignition temperature due to an increase in the oxide thickness occurring during the heating prior to ignition.

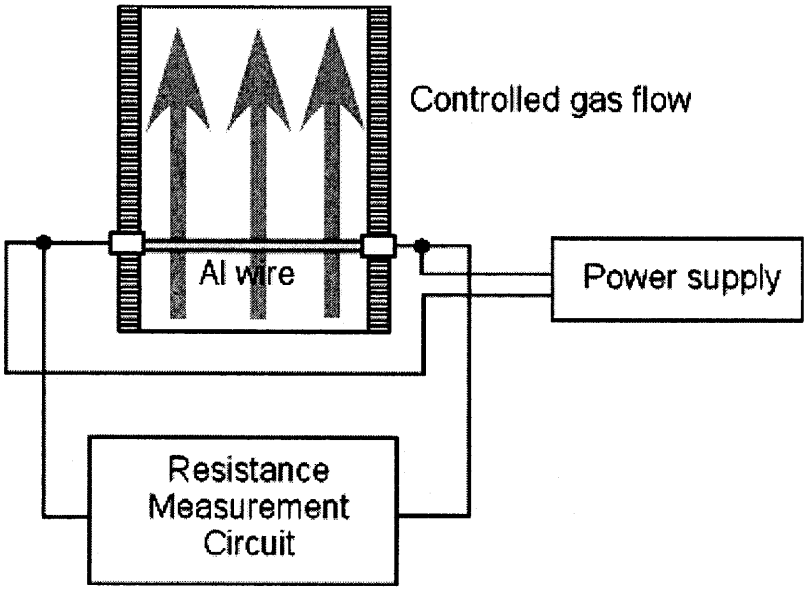

Figure 1.2 Schematic diagram of a wire ignition experiment used in Ref. [9] to determine aluminum ignition temperature.

1.2.3 Ignition of Bulk Aluminum Samples

A series of thorough experiments aimed to determine the ignition temperature of aluminum has been reported by Yuasa and co-workers [10]. In these experiments, illustrated in Fig. 1.3, a 10 mm diameter and 10-mm height aluminum sample in a refractory sample holder was placed in a furnace. The sample temperature was monitored using a thermocouple.

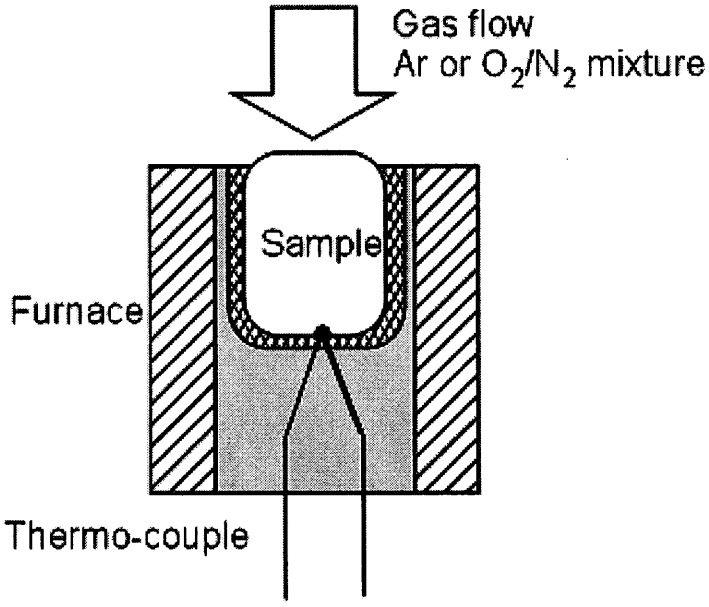

Figure 1.3 Schematic diagram of a bulk sample ignition experiment used in Ref. [10] to determine aluminum ignition temperature.

Two types of ignition experiments were performed. In one experiment, the sample was pre-heated to a desired temperature while being subjected to a flow of argon. The pre-heating was meant to destroy the continuity of the natural oxide film at the surface of the sample. After a desired stable temperature was achieved, the argon flow was replaced with a flow of an oxygen/nitrogen gas mixture. The ignition occurred after a certain delay following the introduction of the oxidizing gas flow. The ignition was

identified optically as an instant when the gas at the surface of the sample became incandescent. Spectroscopic measurements showed that the produced radiation included Al lines and AlO bands. Critical ignition temperatures determined in these experiments increased from 1650 to 1950 °C as the ambient pressure increased from 10 to 100 kPa. At 40 kPa, the maximum pressure of the continuous heating experiments (see below), the ignition temperature was approximately 1800 °C.

In the second experiment, no efforts were made to alter the natural oxide film on the aluminum surface. The sample was continuously heated in an oxidizing (O_2/N_2) gas flow and the temperature of the sample at the instant of ignition was recorded. These experiments were performed at the pressures of 8 and 41 kPa. No significant pressure effect on the ignition temperature was observed. The ignition temperatures decreased from 2050 °C to 1650 °C when heating rates increased from 2 to 9 °C/s.

1.2.4 Ignition of Aluminum Nanopowders

Recently, aluminum nanopowders became available and attracted significant interest in the advanced energetics community. Several investigations have determined the ignition temperatures of such very fine aluminum powders during their slow heating in the furnace of a thermal analyzer. A simplified diagram illustrating such experiments is shown in Fig. 1.4. A small amount of powder, typically, 5 – 10 mg, is placed in a jar and is being heated in a very slow flow of oxygen. During heating, the powder mass is continuously monitored (thermo-gravimetric analysis). At the same time, the temperature of the powder can be monitored and compared to the temperature of a reference inert sample placed in the same furnace (differential thermal analysis).

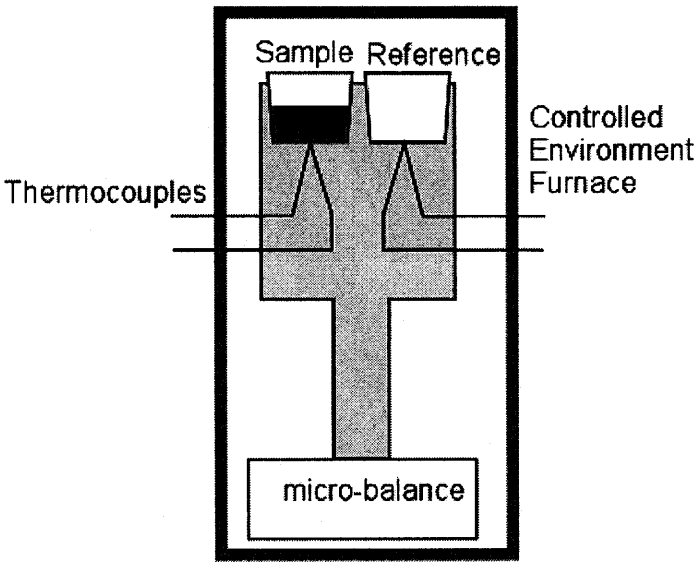

Figure 1.4 Schematic diagram of a thermal analysis experiment used in Refs. [11-13] to determine ignition temperatures for aluminum nanopowders and flakes.

Both nanopowders of aluminum [11-13] and flake-shaped aluminum powders that also have a large specific surface were investigated using this technique. Ignition was detected by a strong heat effect and rapid mass increase. The observed mass increase corresponded to the complete aluminum oxidation. The onset of the rapid heat release was identified as the ignition instant. Both aluminum nanopowders and flakes were observed to ignite at fairly low temperatures, between 560 and 800 °C.

1.2.5 Summary of Measured Aluminum Ignition Temperatures

In addition to the experiments with pre-heated furnaces described above, shock tubes, and other techniques were used to quantify the ignition temperatures of aluminum powders. Review of various experimental reports showed a wide range of the measured ignition temperatures for different aluminum samples. The direct comparisons are difficult because of the significant differences in the experimental conditions, such as pressure,

sample size and shape, thickness of the natural oxide film, specific gas composition, and heating rate. However, it was found instructive to plot the experimental ignition temperatures of aluminum measured at pressures close to 1 atm as a function of the sample size, [5, 6, 9, 10, 13-20], as shown in Fig. 1.5. The trend observed in Fig. 1.5, shows that very fine aluminum powders with a large specific surface ignite at much lower temperatures than bulk aluminum samples. Most importantly, the aluminum powders in the size ranges widely used in energetic materials, i.e., 0.1 – 100 μm, can ignite over a remarkably wide range of temperatures. At the same time, knowledge of the specific ignition temperature is crucial for the accurate modeling of performance of a practical combustion system. Figure 5 shows that while aluminum particle size clearly affects its ignition temperature, for some size ranges, e.g., 10 – 100 μm, particles of similar sizes were observed to ignite at very different temperatures. Thus, other experimental conditions must be considered to predict the ignition temperature for any specific application.

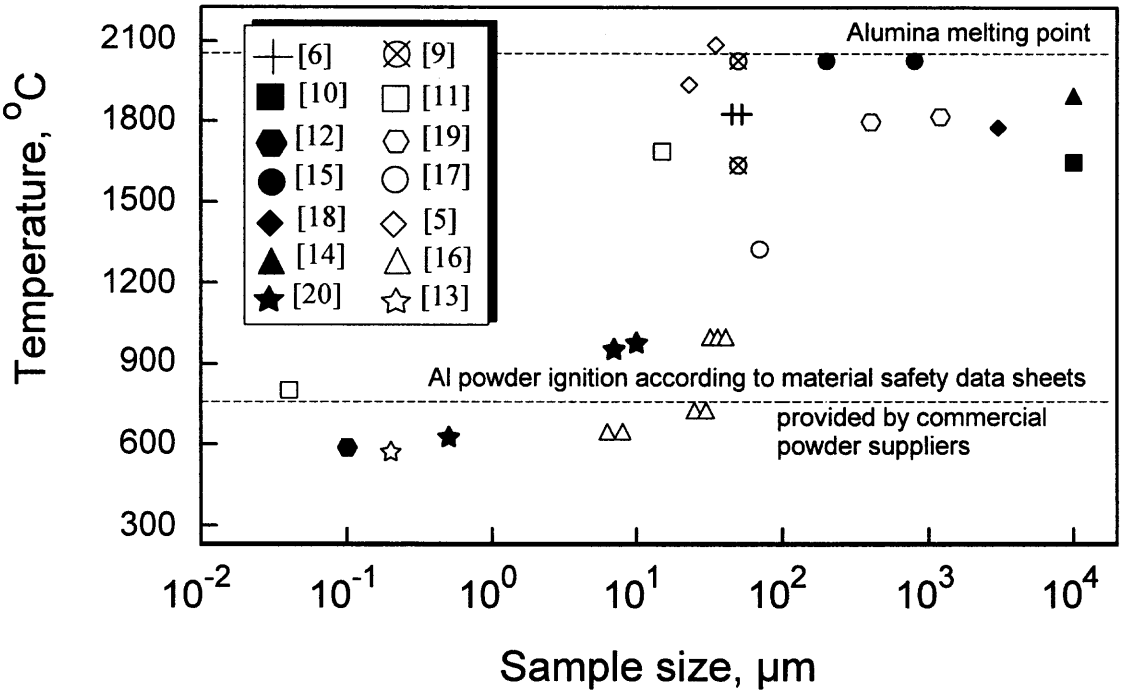

Figure 1.5 Experimentally determined temperatures of aluminum ignition as a function of the used sample size.

1.3 Current Models of Aluminum Ignition

Many different approaches to describe aluminum ignition have been presented in the literature. However, it is possible to reduce most available models to three main types. Each approach is briefly described and discussed below.

1.3.1 Fixed Ignition Temperature

This simple and the most popular model is based on a number of experimental reports showing that aluminum particles ignite in the vicinity of the melting point of Al_2O_3 (i.e., 2053 °C). Hence, it was suggested that the oxide film that is always present on the aluminum surface prevents ignition until it melts. After the oxide melts, it forms isolated islands instead of the continuous coverage. The surface of aluminum becomes exposed

to the oxidizer and the particle ignites. The protective properties of aluminum oxide are well known [21]. The approach to describe aluminum ignition by introducing a constant ignition temperature is very simple and therefore, appealing. It has been recognized that a better agreement with experiments can be achieved in most cases if the ignition temperature is selected somewhat below the Al_2O_3 melting point. In Refs. [22, 23], the ignition temperatures were arbitrarily chosen between 1700 and 2100 °C. For many experiments in which larger aluminum particles were used, this approach produced quite satisfactory results. However, as it is clear from Fig. 1.5, this approach is inadequate for finer aluminum particles, which are likely to be used in many practical combustion systems. To address this discrepancy, some authors chose to select a much lower critical ignition temperature, e.g., 1077 °C [24].

1.3.2 Stress in the Oxide Scale

This model introduced by Rozenband and Vaganova [25] and further developed in Refs. [10] and [26] suggests that the protective oxide coating breaks up due to mounting mechanical stresses. Similarly to the described above model, breakage of the oxide layer exposes bare aluminum surface to the oxidizer and leads to the ignition. Whereas the model of the oxide scale break-up has been advanced significantly, the mechanical properties of the heated alumina are poorly known. Therefore, accurate predictions of the experimental ignition temperatures are impossible. Recent analysis [26] showed that the most significant stress in the oxide film develops just after the melting of aluminum, i.e., immediately above 660 °C. At elevated temperatures, e.g., above 1100 °C, the deformations of Al_2O_3 result in the grain boundary sliding causing a brittle to ductile

transition [27]. Therefore, the stresses in the oxide film are relaxed and the rupture of the oxide film is unlikely to occur. Therefore, this model does not seem to be able to adequately describe ignition of aluminum powders observed at either very low (560-600 °C) or relatively high (>1500 °C) temperatures.

1.3.3 Exothermic Growth of Oxide Film

In this model, the oxide scale is considered as growing in an oxidizing environment. The heat release due to oxidation is estimated and compared to external particle heating or heat losses. Ignition is predicted by a respective particle heat transfer model including the enthalpy of oxidation. Analysis of the specific heat transfer model typically includes such terms as convective heat transfer and an exothermic oxidation reaction limited by the diffusion of reagents through a growing oxide film [9, 28-30]. Such an analysis immediately implies that an effect of the particle size on the ignition temperature could be predicted. A rate of oxide film growth is typically described by an Arrhenius-type term, e.g.,

$$\frac{dh_{ox}}{dt} = B\frac{C_{oxidizer}^{p}}{h_{ox}^{n}}\exp\left(-\frac{E}{RT}\right) \tag{1.1}$$

where h_{ox} is the thickness of the oxide film, t is time, T is temperature, C is concentration, R is the universal gas constant, and E and B are activation energy and pre-exponent, respectively. The exponents p and n represent the effect of the oxidizer pressure and oxide thickness on the oxidation law. Often, both exponents are assumed to be equal to one, suggesting a parabolic law of oxidation. Other choices have been also discussed in the literature based on the experimental data collected for different oxidation temperature

ranges [31]. The model requires that the values of E and K are determined from independent sources. Typically, these values are extracted from the aluminum oxidation studies. However, the analysis of the literature shows great discrepancies between the values used and reported by different researchers. Some of the examples of the values of the activation energy used in the aluminum ignition models [9, 30, 32-36] are given in Table 1.1. The same table also shows some of the other activation energy values reported in the relevant aluminum oxidation studies [37-40]. Note that a small change in the activation energy greatly affects the oxidation kinetics described by an exponential function. Therefore, an adequate selection of the values of E and K is critical for an accurate description of the ignition processes of aluminum. However, review of the available literature and some of the recent studies (e.g., [41]) indicate that it is impossible to select a single Arrhenius-type function to describe the growth of the aluminum oxide film. Many different alumina polymorphs exist in different temperature ranges and a more detailed oxidation model is necessary to describe the growth of aluminum oxide scale in the range of conditions appropriate for the ignition experiments.

Table 1.1 Activation Energies Relevant for Description of Aluminum Oxidation.

	Activation energy, kJ/mol	Reference
Activation energies used by different researchers to describe oxidation	71	9, 29
	83.8	32
	95.5	30, 35, 36
	149.6	33
Activation energies for heterogeneous aluminum oxidation reported by different researchers	77.9	37
	146	38
	394	39
	418	40

CHAPTER 2

EFFECT OF POLYMORPHIC PHASE TRANSFORMATIONS WITHIN Al_2O_3 FILM ON THE OXIDATION KINETICS OF ALUMINUM POWDERS

2.1 Introduction

The processes of aluminum combustion have been studied extensively, e.g., [22, 42-43]; however, some of the processes that are crucial for accurate modeling of aluminized energetic materials remain poorly understood. The ignition of aluminum particles is one such process. Aluminum oxide film, always present on the particle surface, is well known for its protective properties. It prevents oxidation of aluminum and its alloys at low temperatures. At elevated temperatures, the properties of the oxide must change leading up to ignition, this evolution of the oxide film during particle heating has never been systematically studied.

This chapter presents a brief summary of the changes known to occur in aluminum oxide films and the experimental study of oxidation of aluminum powders with different particle sizes. The results are analyzed to identify the processes affecting aluminum oxidation rates at different temperatures.

2.2 Background: Phase Changes in Growing Alumina Scale

Aluminum oxide phases and phase changes have been extensively studied and excellent reviews, e.g., [44] are available in literature. Significant progress has also been made recently in understanding the growth kinetics of alumina layers at elevated temperatures [45-47] and in the quantification of related mass transfer coefficients, e.g. review [48].

Because this information has not been used extensively by combustion researchers, a brief summary is given below.

It is known that the oxide scale forming on the surface of aluminum at low (room) temperatures consists of a thin layer of amorphous alumina [45, 46]. The thickness of this "natural" oxide coating (also referred to as "limiting" oxide film thickness) has been evaluated by different researchers to vary from about 0.5 nm [47] to 4 nm [49]. Most of the authors suggest that the aluminum powders are coated with a 2-3 nm thick layer of aluminum oxide, e.g., [50-52]. The common route of phase transformations in alumina film grown on aluminum surface by thermal oxidation has been established in Ref [44] as:

$$\text{Amorphous film} \rightarrow \gamma \rightarrow \delta \rightarrow \theta \rightarrow \alpha\text{-}Al_2O_3$$

The densities of these alumina polymorphs are different from one another, as shown in Table 2.1. Thus, significant changes in the oxide film morphology are expected when the density changes abruptly, i.e., when amorphous oxide film transforms into a crystalline polymorph and when stable α-Al_2O_3 forms from other transition alumina phases, e.g., γ, δ, or θ.

Table 2.1 Densities of Alumina Polymorphs Formed in During Thermal Oxidation [44].

Polymorph	Density, g/cm^3
Amorphous Al_2O_3	3.0 – 3.1
γ, δ, θ – Al_2O_3	3.60 – 3.67
α-Al_2O_3	3.99

It has been recently shown that amorphous alumina is thermodynamically more stable on aluminum surface than any crystalline polymorphs until the thickness of the layer reaches a critical value [45]. The critical thickness depends on the crystallographic orientation of the aluminum substrate and varies somewhat as a function of temperature. In the temperature range of 20 – 600 °C, the specific values of the critical thickness are close to 0.5, 2.5, and 5 nm for the 111, 100, and 110 crystallographic faces of aluminum, respectively [45]. After the critical thickness of the oxide layer is exceeded, amorphous alumina becomes metastable and transitions to γ-alumina. The resulting γ-alumina is stabilized due to its small crystallite size [53]. When the temperature increases to about 950 – 1250 °C [44], γ-alumina transforms into the thermodynamically stable α-alumina. This transformation may proceed directly or *via* a number of intermediate phases such as δ-, and θ-alumina [44]. Formation of α-alumina crystallites with larger size (exceeding 30 nm) and higher density results in the overall densification of the alumina scale [44, 50].

The rate of growth of the amorphous oxide layer is limited by the outward diffusion of aluminum cations [47]. A network of grain boundaries within the polycrystalline γ-alumina scale provides diffusion paths for oxygen [48]. Thus, inward

oxygen diffusion becomes the rate limiting mechanism for the growth of γ-alumina scales [47-48]. Grain boundary diffusion of oxygen towards the Al-Al_2O_3 interface remains the oxidation rate limiting process for the polycrystalline α-alumina scales. However, because of the coarser crystallites and higher oxide density, the rate of grain boundary diffusion is reduced compared to that typical for γ-alumina. Therefore, the diffusion rate constant changes as a result of the $\gamma \rightarrow \alpha$ alumina transition.

2.3 Materials and Method

Four types of aluminum powders were used in this study. Representative electron microscope images of the particles are shown in Fig. 2.1. Two fine powders have nearly ideal spherical particles: Alfa Aesar, nominal sizes of 3 - 4.5 μm (97.5 % Al) and 10 - 14 μm (98 % Al). A coarser aluminum powder, Alfa Aesar -40 +325 mesh, has particles with irregular shapes. The fourth sample used was aluminum flakes by Iowa Pyro Supply, -325 mesh. The flakes are from 20 to 200 nm thick.

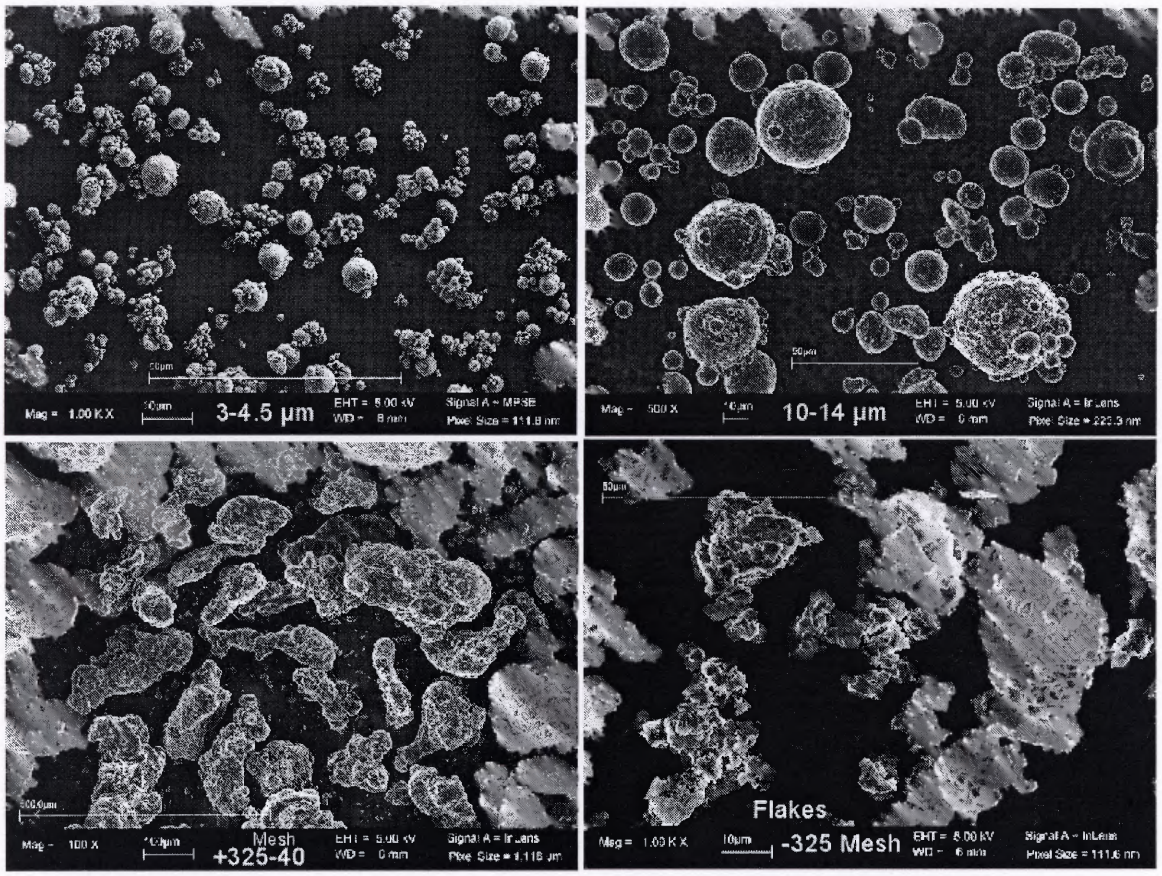

Figure 2.1 SEM images of the aluminum powders used in oxidation experiments.

The particle sizes were analyzed using low angle laser light scattering (LALLS; LS230 Beckman-Coulter Particle Analyzer) for all samples except flakes. Specific surfaces of the finer powders, S_{BET}, were measured by the Brunauer-Emmett-Teller (BET) method using a NOVA 3000 High Speed Gas Sorption Analyzer. The BET diameters, d_{BET}, were calculated as $d_{BET} = \frac{6}{S_{BET}\rho_{Al}}$, where ρ_{Al} is the density of aluminum. The measured particle sizes are presented in Table 2.2.

Table 2.2 Characteristics of Used Aluminum Powders.

Powder ID	Specific surface, S_{BET}, m^2/g	BET diameter, d_{BET}, μm	Laser Light Scattering: Area mean diameter, μm
Spheres 3 - 4.5 μm	1.15	1.93	3.9
Spheres 10 - 14 μm	0.41	5.42	16.4
-40+325 Mesh	N/A	N/A	201.1
Flakes -325 Mesh	7.41	N/A	N/A

The oxidation of aluminum powder in oxygen was studied by differential thermal analysis (DTA) with simultaneous thermo-gravimetric analysis (TGA) using a Netzsch Simultaneous Thermal Analyzer STA409 PC. The instrument was calibrated for temperature with the melting points of a set of metal standards resulting in a temperature accuracy of ±1 °C, 25-30 mg samples contained in alumina crucibles were heated from room temperature to 1490 °C with heating rates varying in different experiments from 5 to 40 °C /min. The oxygen flow rate was 50 ml/min. To recover the intermediate products, in some experiments the sample oxidation was interrupted at a particular temperature, the oxygen atmosphere was replaced with argon, and samples were cooled to room temperature. Recovered samples of intermediate products were analyzed by x-

ray diffraction (XRD) on a Philips X'pert MRD x-ray diffractometer using unfiltered Cu-Kα radiation (1.54187 Å wavelength, 45 kV, 40 mA). The samples were thinly coated on a single-crystal Si sample holder using hexane as a dispersion medium; diffraction patterns were collected from 15° to 70° 2Θ.

2.4 Results

The TGA curves in Fig. 2.2 show the sample mass increase as a function of temperature for different aluminum powders heated at different heating rates. At temperatures below ~ 550 °C, the oxidation is relatively slow; a significant mass increase (of about 5%) was observed only for aluminum flakes, which have the highest specific surface of the powders studied (comparable to that of aluminum nano-powders, e.g., [54]). Accelerated oxidation was consistently observed for all samples in a narrow temperature range from 550 to 650 °C. Oxidation slowed down significantly just before the aluminum melting point. Insets in Fig. 2.2 show this region of the TGA curves with a magnified vertical scale. For the aluminum flakes heated at 5 K/min, this increased oxidation rate resulted in the oxidation of more than a third of all the available aluminum. The sample of Al flakes heated at 10 K/min ignited during the experiment at about 560 °C as illustrated by a very sharp weight increase. This stepwise oxidation was completed for all samples by about 650 °C. At this temperature, the oxidation rate was at its minimum and started to continuously increase while the temperature was increased up to about 1000 – 1100 °C. Note that the complete oxidation to Al_2O_3 would result in a mass increase of about 88 %. In the case of flakes, nearly all the aluminum was oxidized below 1000 °C, and the oxidation rate slowly decreased as the temperature continued to increase.

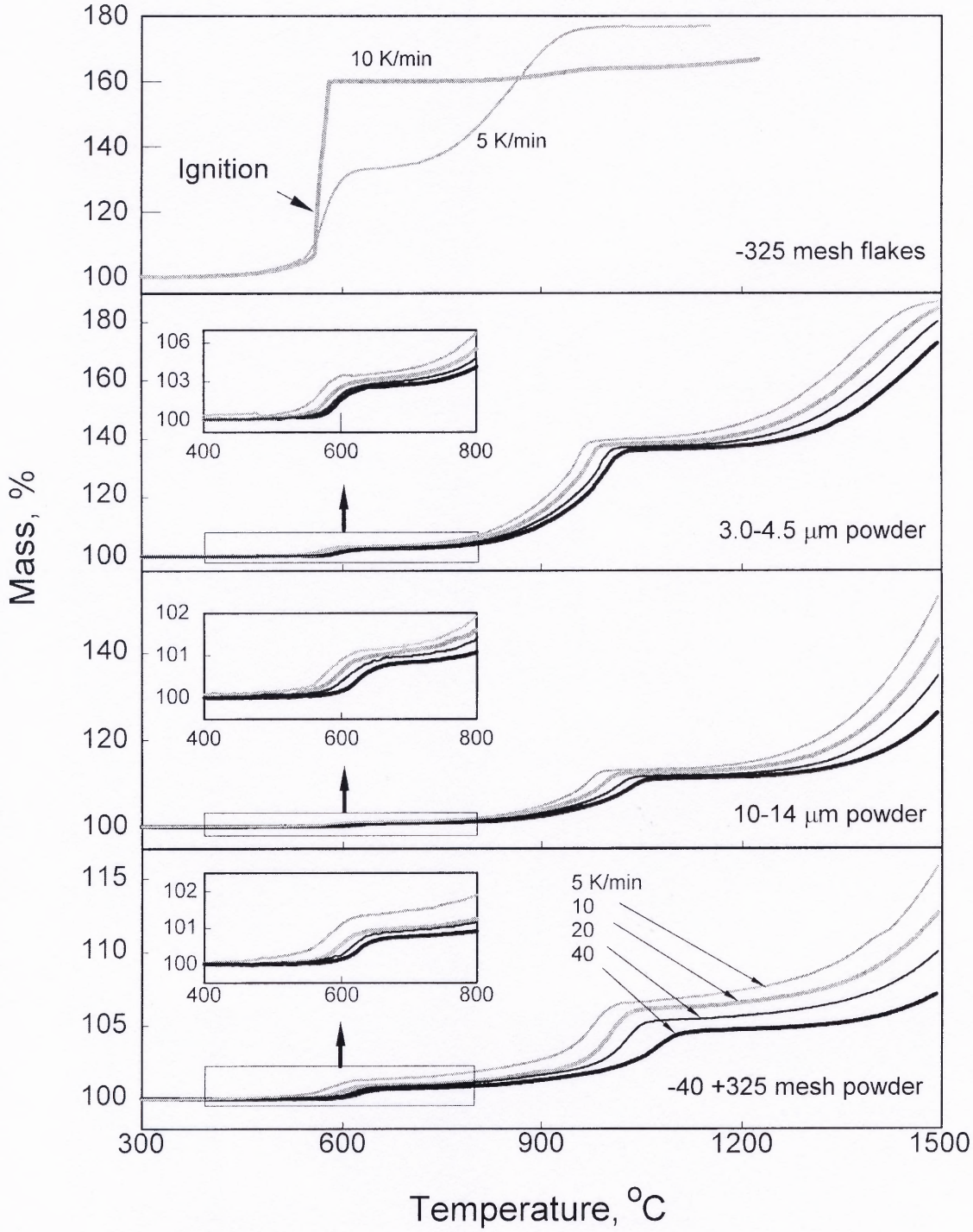

Figure 2.2 Summary of TGA measurements for oxidation of different aluminum powders.

For other powders, a fairly thick oxide layer was formed by about 1100 °C, at which point the oxidation rate decreased abruptly. Very low oxidation rates are inferred for all of the powders by the nearly horizontal portions of the TGA curves between about 1100 and 1200 °C. Continuing temperature increase resulted again in an accelerated oxidation. The measurements above 1450 °C were generally less reproducible and should be regarded with caution because of the approaching limit of the temperature calibration range (1500 °C).

The qualitative oxidation behavior described above was consistently observed for all powders. At higher heating rates, the observed oxidation steps consistently shifted towards higher temperatures as illustrated in Fig. 2.2. The processing of the experimental data using isoconversion methods was attempted in order to evaluate the activation energies of different oxidation steps, e.g., in the vicinity of 600 and 1050 °C. This processing was not successful: the values of the obtained activation energies were inconsistent from sample to sample in spite of qualitative similarities between the TGA curves for different powders.

Below, different regions of the TGA curves are referred to in terms of oxidation stages. These stages are shown schematically in Fig. 2.3 using a typical TGA curve and its derivative, which is directly proportional to the rate of oxidation. The first stage refers to the slow oxidation at temperatures below ~ 550 °C. The second stage describes the stepwise mass increase in the temperature range of 550 – 650 °C. The third stage describes the temperature interval over which the oxidation rate continuously increases, from about 650 to 1000 – 1100 °C. The increase of the oxidation rate is abruptly

terminated as is clearly shown by the derivative of the TGA curve in Fig. 2.3. Finally, the fourth oxidation stage describes the increase of the oxidation rate above 1100 °C.

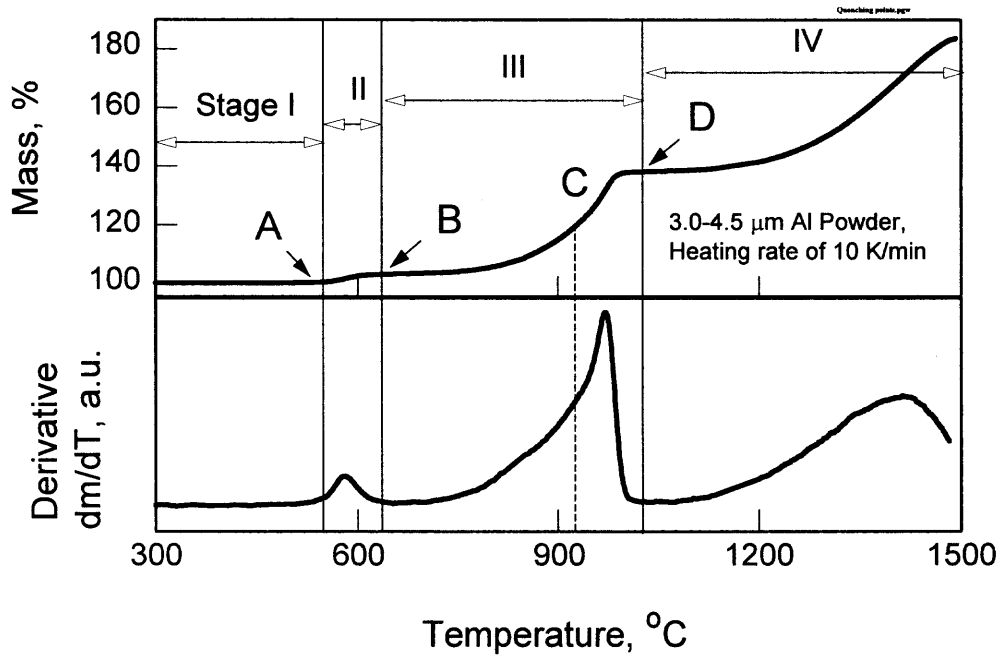

Figure 2.3 Stages in oxidation of aluminum powders: a typical TGA curve and its derivative as a function of temperature. Points A, B, C, and D show temperatures at which the samples were recovered for XRD analyses.

In order to understand the processes causing the observed changes in the oxidation rate and to identify intermediate oxidation products, several samples of spherical aluminum with 3 - 4.5 μm particle size were heated in oxygen at 10 °C/min to selected temperatures, cooled in argon, and analyzed by XRD. Samples were recovered from 540, 635, 926 and 1020 °C, as illustrated in Fig. 2.3 by points A, B, C, and D, respectively. Since the mass increase for the spherical powder during the first oxidation stage was very small, a sample of aluminum flakes containing significantly larger amounts of oxide (see Fig. 2.2) was also heated to 540 °C and recovered for analysis.

The x-ray patterns of samples oxidized to different temperatures are shown in Fig. 2.4. The patterns are not shown for the samples oxidized to 540 °C because no peaks of Al_2O_3 could be identified for either the spherical powder or the flakes. Weak peaks of γ-Al_2O_3 in addition to strong peaks of metallic aluminum are observed for the sample recovered from 635 °C. The peaks of α-Al_2O_3 become noticeable only by the end of the third oxidation stage, at 926 °C. At this point, the peaks of γ-Al_2O_3 become stronger and a set of peaks corresponding to θ-Al_2O_3 appear. The peaks of γ-Al_2O_3 disappear from the XRD patterns upon completion of the third oxidation step, at 1020 °C. At this point, the peaks of α-Al_2O_3 become very strong, and only minute amounts of θ-Al_2O_3 remain.

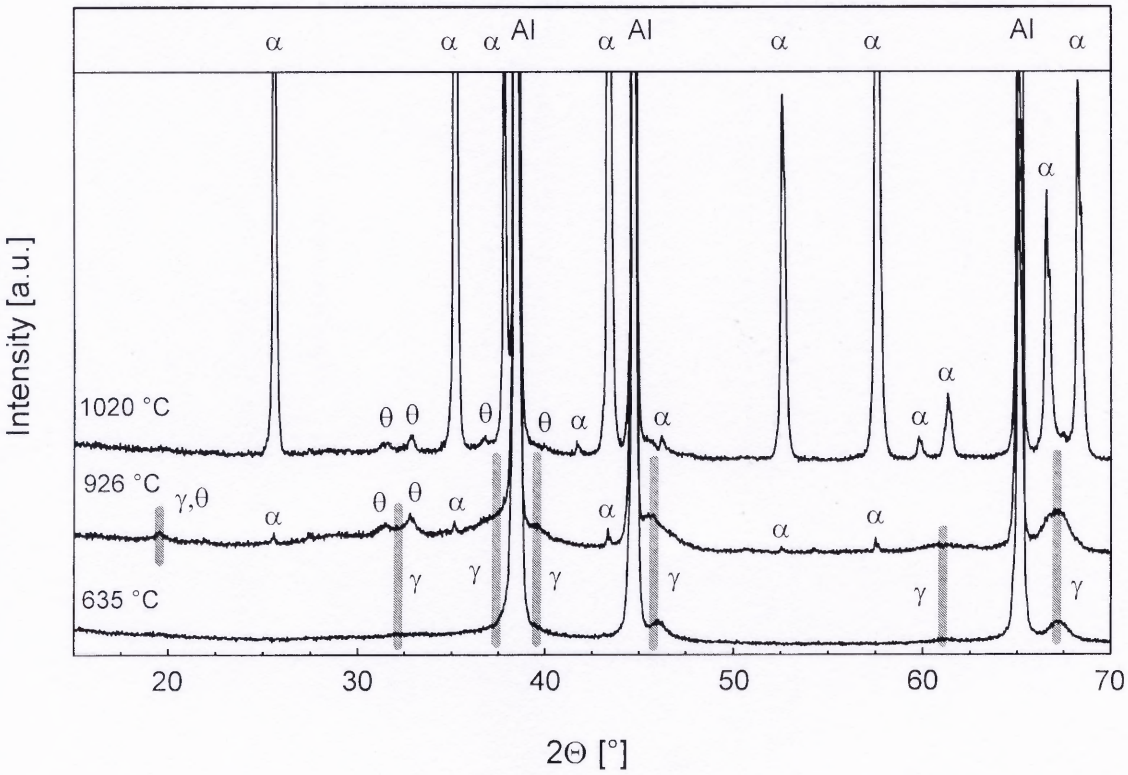

Figure 2.4 XRD patterns for partially oxidized aluminum powder samples. The observed XRD peaks are identified for different polymorphs of Al_2O_3.

The thickness of the oxide layer at different oxidation stages was estimated from the increase in the overall sample mass as observed in the TGA curves. For this simple estimate, the oxide was assumed to uniformly cover the powder surface area determined by BET. The thickness of oxide film for the flakes was also estimated using the BET specific surface measurements and assuming that the flake thickness is significantly smaller than its length and width. Note that specific surface of the coarse, -40 +325 mesh powder was smaller than could be determined by BET measurements; consequently, the oxide thickness could not be estimated for this powder, either. Based on the phases identified by XRD (see discussion below), the Al_2O_3 layer thicknesses by the end of different oxidation stages were estimated using the density of amorphous alumina for the first oxidation stage (ρ_{am} = 3050 kg/m^3 [44]), the density of γ-Al_2O_3 for the second stage (ρ_γ = 3660 kg/m^3 [44]), and the density of α-Al_2O_3 for the third and fourth oxidation stages (ρ_α = 3990 kg/m^3 [44]). The fourth oxidation stage was never completed in these experiments; therefore, the final oxide thickness was estimated at 1450 °C for all powders. The estimated thicknesses of the oxide layers corresponding to the ends of the respective oxidation stages are summarized in Table 2.3.

Table 2.3 Experimental Oxide Thickness Estimated Based on the Measured Weight Increase and Powder Specific Surface From the BET Measurements.

Powder ID	Heating Rate, °C/min	Estimated oxide thickness, nm			
		End of Stage I	End of Stage II	End of Stage III	Stage IV (1450 °C)
Flakes -325 Mesh	5	7.4	27.8	N/A, nearly complete oxidation	
	10	8.9		N/A, ignition	
Spheres 3-4.5 μm	5	5.2	20.0	213	707
	10	3.8	18.1	202	567
	20	3.6	16.6	197	480
	40	3.9	15.2	192	395
Spheres 10-14 μm	5	4.7	17.2	176	613
	10	4.2	16.3	168	478
	20	4.6	15.4	155	379
	40	4.0	13.8	149	287

2.5 Discussion

The specific processes responsible for the individual oxidation stages of aluminum powders must be understood in order to accurately model aluminum ignition. The oxidation stages observed in this work are generally consistent with previous reports on aluminum powder oxidation, e.g., [55-59]. Experimental results obtained in this work systematically cover powders with a range of particle sizes and morphologies. This information can be used to develop a qualitative and quantitative description of the oxidation processes involved.

As prepared, aluminum powders are coated with an amorphous alumina layer [44-47]. Therefore, growth of this layer is expected to occur during the initial oxidation stage. The growth of amorphous oxide during stage I oxidation is also consistent with our inability to identify any alumina phases by XRD, even for partially oxidized sample of aluminum flakes that gained up to 5 % of its initial mass during stage I oxidation (see Fig. 2.2).

The amorphous alumina layer becomes metastable when its thickness exceeds a critical value [45]. A sharp increase in the oxidation rate is indeed observed for both spherical powders when the thickness of the oxide exceeds 3.6 - 5.2 nm (see Table 2.3; end of stage I data). This experimentally observed oxide thickness agrees well with the maximum critical thickness of amorphous alumina reported in Ref. [45]. Thus, the transition from stage I to stage II oxidation can be interpreted as the transformation of amorphous alumina to a crystalline alumina polymorph. Note that by end of stage I oxidation, the estimated oxide film thickness for the flake samples is slightly higher than that observed for spherical powders. This minor discrepancy could be caused by the

particle surface morphology that was not accounted for in our estimate for the oxidizing surface for flakes.

According to Ref. [44], a common route for the formation of stable α-Al_2O_3 from amorphous alumina film is: *amorphous* $\rightarrow \gamma \rightarrow [\delta] \rightarrow [\theta] \rightarrow \alpha$-$Al_2O_3$. The intermediate phases shown in brackets may or may not be produced. The formation of γ-Al_2O_3 is expected during the second oxidation step. The density of γ-Al_2O_3 is about 20% higher than that of amorphous oxide. At the same time, the smallest crystallite size of γ-Al_2O_3 has been observed to be in the range of several nanometers, i.e., comparable to the thickness of the oxide film existing at this point on the aluminum surface. Thus, it is suggested that the newly formed γ-Al_2O_3 scale does not fully cover the aluminum particle surface that was previously protected by continuous amorphous alumina film. The formation of bare aluminum spots, and their immediate oxidation could cause the rapid rate increase of aluminum oxidation at relatively low temperatures in stage II, see Figs. 2.2, and 2.3. As oxidation continues, the openings in the γ-Al_2O_3 layer heal until a continuous γ-Al_2O_3 coverage forms on the particle surface. This causes the transition to a slower oxidation at the beginning of the observed stage III. According to our measurements, the healing of the γ-Al_2O_3 layer is completed when its equivalent thickness as estimated from the mass increase approaches 15-20 nm. The XRD data confirm the presence of γ-Al_2O_3 by the end of stage II, in agreement with the proposed oxidation mechanism. Note that the detection of broad and relatively small peaks produced by the thin γ-Al_2O_3 layer is difficult. Therefore, only the fine powders with larger relative fractions of oxides were examined in this study using XRD.

Further temperature increase results in continuous growth of the γ-Al_2O_3 layer and its eventual transformation to α-Al_2O_3 *via* the intermediate transition alumina phases. The presence of θ-Al_2O_3 is clearly established by XRD for the sample recovered from the partially completed stage III (see Figs. 2.3 and 2.4). This indicates that stage III may need to be divided further into sub-stages, in which transitions between γ-Al_2O_3 and other metastable alumina polymorphs occur. Note that the densities of the γ, δ, and θ phases are all close to one another [44], so no dramatic changes in the grain boundary oxygen diffusion rate are expected. This diffusion process controls the oxidation rate, which remains almost constant while these polymorphs are being formed. By the end of stage III, the rate of oxidation is dramatically decreased, which can be explained by the formation of a significantly denser and coarser crystallites of α-Al_2O_3. The densification of the alumina layer can readily explain the decrease in the rate of oxygen diffusion and the resulting low rate of alumina growth at the beginning of the stage IV. The XRD pattern once again supports this mechanism showing formation of large quantities of α-Al_2O_3, no γ-Al_2O_3, and only traces of θ-Al_2O_3 at the beginning of stage IV (see Fig. 2.4). A further temperature increase results in continuously increased rates of oxygen diffusion and oxidation, as observed during the remainder of stage IV.

2.6 Conclusions: Proposed Sequence of Processes in Alumina Scale During Aluminum Oxidation

Oxidation of aluminum powders at elevated temperatures was studied experimentally. Four oxidation stages were identified based on thermogravimetry in the temperature range from 300 to 1500 °C. The analysis of partially oxidized samples recovered from

specific intermediate temperatures and a review of the available literature on alumina polymorphs formed at different temperatures were used to suggest the following simplified oxidation sequence. This sequence is illustrated schematically by a diagram in Fig. 2.5 that also shows a characteristic thermo-gravimetric analysis (TGA) curve of oxidizing aluminum powder.

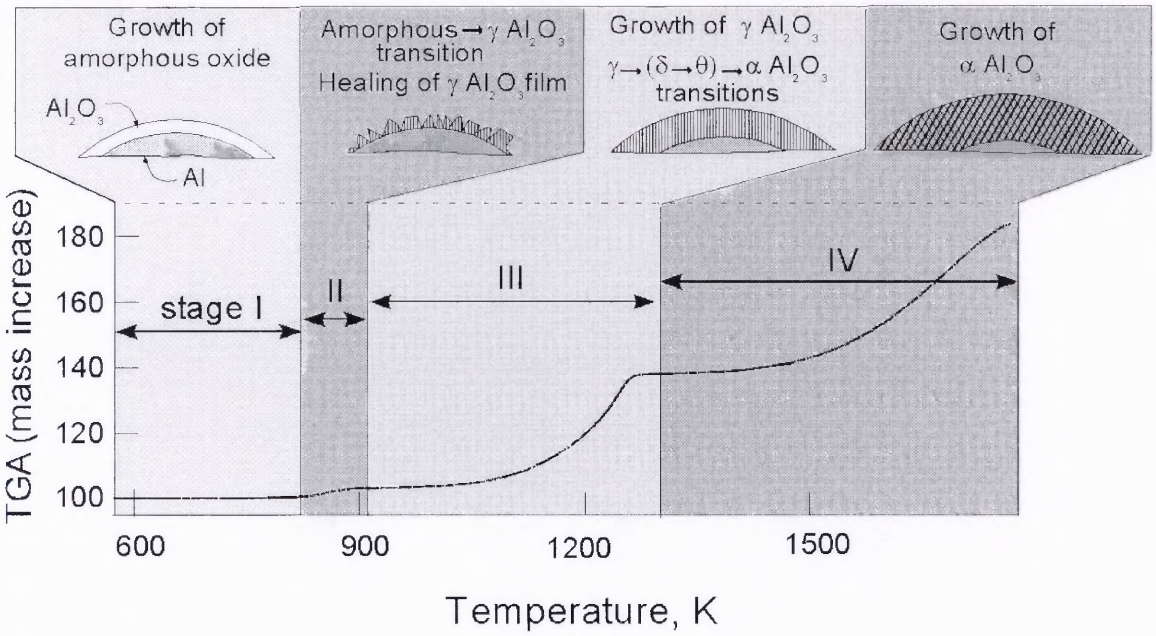

Figure 2.5 Change in mass of the aluminum powder oxidizing in a thermal analyzer. Different stages of oxidation are indicated and the respective changes in the growing alumina scale are shown schematically.

During stage I, from 300 to about 550 °C, the thickness of the natural amorphous alumina layer on the particle surface increases. The rate of this process is controlled by the outward diffusion of Al cations. A transformation of amorphous alumina into γ-Al_2O_3 occurs at about 550 °C, when the oxide layer thickness exceeds the critical thickness of amorphous alumina of ~ 4 nm. The density of the γ-Al_2O_3 is greater than that of amorphous alumina, and the newly formed γ-Al_2O_3 nano-crystallites produce a

monolayer covering the aluminum surface only partially. A bare aluminum surface is produced as a result of the amorphous - γ-Al_2O_3 transformation. The rate of oxidation increases rapidly at the beginning of stage II as shown in Fig. 2.5. As the openings in the oxide coating heal, the rate of oxidation decreases. Eventually, a regular polycrystalline layer of γ-Al_2O_3 forms by the end of stage II. The growth of γ-Al_2O_3 continues in stage III for which the oxidation rate is limited by the inward grain boundary diffusion of oxygen anions. Growth of the γ-Al_2O_3 layer can be accompanied by phase transformations into other transition polymorphs, such as δ-Al_2O_3 and θ-Al_2O_3, which have densities very close to that of γ-Al_2O_3. Such transitions are not expected to significantly affect the oxidation rate. Stage III ends when the increased temperature destabilizes the transition alumina polymorphs. The stable and denser α-alumina polymorph starts forming by the end of stage III; stage IV is considered to start when the oxide scale is completely transformed to α-alumina. When first individual α-Al_2O_3 crystallites begin to form by the end of stage III, the thickness of the γ-Al_2O_3 layer decreases, and the oxidation rate increases momentarily. Once most of the oxide layer is transformed to coarse and dense α-Al_2O_3 crystallites resulting in continuous polycrystalline coverage, grain boundary diffusion slows down, and the oxidation rate decreases rapidly. Final oxidation stage IV is characterized by the formation and growth of the α-Al_2O_3 oxide.

CHAPTER 3

EFFECT OF POLYMORPHIC PHASE TRANSFORMATIONS WITHIN ALUMINA LAYER ON THE IGNITION OF ALUMINUM PARTICLES

3.1 Introduction

Oxidation kinetics of aluminum powders with different particle sizes and morphologies have recently been studied using thermal analysis [13, 60-61]. It has been determined that all aluminum powders oxidize in several stages. It has also been established that different Al_2O_3 polymorphs form as a result of both continuing oxidation and phase changes during different oxidation stages.

In this chapter, an aluminum ignition model is developed based on the quantification of the sequence of processes occurring during heterogeneous oxidation of aluminum described above. The experimental data presented in the chapter 2 (see also Ref. [13]) are used extensively to obtain quantitative description of aluminum oxidation kinetics. The ignition model developed here is used to describe a wide range of experimental ignition temperatures observed for aluminum powders with different particle sizes.

3.2 Aluminum Oxidation Kinetics

3.2.1 Methodology for Processing TGA Experiments for Oxidizing Aluminum Powders

The oxidation model of aluminum developed here is based on experimental TGA data of aluminum oxidation [13]. The results of thermal analysis are frequently processed to determine the kinetics of the underlying processes using isoconversion methods, e.g., the

method after Kissinger [62, 63]. Such methods can be used if the state of transformation can be clearly identified from the TGA curves, and if the kinetics of each identified process can be described by a single activation energy. In the case of the TGA data from Ref. [13], isoconversion methods were not successful. Despite the similarity of the TGA traces of powders with different particle sizes, the derived activation energies varied. This could indicate that several thermally activated processes overlapped during oxidation. To better distinguish such processes, each individual TGA curve was analyzed separately in the present work.

For simplicity, particles were assumed to be spherical. It was further assumed that at any given time the rate of oxidation is limited by the diffusion of only one species, A, so that the rate of sample mass change, $\dot{m}$, is proportional to the molar rate of diffusion of this species for a single particle, $\dot{N}_A$: $\dot{m} \sim |\dot{N}_A|$. The coefficient of proportionality depends on the stoichiometry of the oxidation reaction, the initial sample mass, and the type of the reaction rate limiting species.

The species A can be different at different oxidation stages. According to the qualitative description of oxidation processes presented above (cf. Fig. 2.5), the rate of oxidation is limited by the outward diffusion of aluminum cations in stage I, and by the inward diffusion of oxygen anions along grain boundaries in stages 2 – 4. The following model describes diffusion for spherical particles in a quasi-steady state approximation. It is assumed that both the particle and the oxide layer are at the same temperature. Thus, the absolute value of the diffusion rate for a single particle is given by the solution of a radial diffusion equation:

$$\left|\dot{N}_A\right| = \frac{\left|C_A^{ox} - C_A^{Al}\right|}{\frac{1}{r_{Al}} - \frac{1}{r_{ox}}} 4\pi D_A \tag{3.1}$$

where D_A is the diffusion coefficient of the species A in the oxide layer; C_A^{Al} and C_A^{ox} are molar concentrations of the species A on the interfaces of the oxide with the aluminum core and the oxidizing gas, respectively; r is the radius and the subscripts Al and ox describe aluminum core and oxide layer, respectively. Assuming that the concentration of species A equals zero at the reaction interface, i.e., either $C_A^{Al} = 0$ or $C_A^{ox} = 0$ we obtain:

$$\left|\dot{N}_A\right| = \frac{C_A}{\frac{1}{r_{Al}} - \frac{1}{r_{ox}}} 4\pi D_A \tag{3.2}$$

where C_A is the concentration of species A at the side of the oxide layer where the source of this species is.

$$\frac{dm}{dT} = \frac{\dot{m}}{\dot{T}} \sim \frac{\left|\dot{N}_A\right|}{\beta} \tag{3.3}$$

where $\beta = \dot{T}$ is the sample heating rate. Expressing $\left|\dot{N}_A\right|$ using Eq.(3.2) gives:

$$\frac{dm}{dT} \sim \frac{C_A D_A}{\frac{1}{r_{Al}} - \frac{1}{r_{ox}}} \frac{1}{\beta} \tag{3.4}$$

Assuming that the diffusion is described by Arrhenius kinetics we obtain:

$$\frac{dm}{dT} = \frac{C_A^* \exp\left(-\frac{E}{RT}\right)}{\frac{1}{r_{Al}} - \frac{1}{r_{ox}}} \frac{1}{\beta} \tag{3.5}$$

where C_A^* is the combined oxidation constant depending on the reaction stoichiometry, the initial sample mass, and the type of the species A. Each process occurring during oxidation can be characterized by its specific activation energy. The values of these process-specific activation energies can be found from the differential TGA curves (i.e., from $\frac{dm}{dT}$ as a function of temperature):

$$\frac{E}{RT} = \ln C_A^* - \ln\left(\frac{dm}{dT}\right) - \ln(\beta) - \ln\left(\frac{1}{r_{Al}} - \frac{1}{r_{ox}}\right) \tag{3.6}$$

The radii r_{Al} and r_{ox} at different temperatures are also readily derived from the current sample mass m obtained from the TGA, as described in the Appendix. Therefore, the right side of Eq. (3.6) depends only on the experimental sample mass. The TGA data can now be represented by a function, *Y(TGA)*, equivalent to the right side of Eq. (3.6). This function is usefully plotted *vs.* inverse temperature. Portions of this function approaching straight lines can be interpreted as parts of the oxidation process for which the activation energy remains constant and equal to the slope of the line. Data for experiments with different heating rates and different particle sizes can now be compared directly. The activation energies determined from different experiments should coincide if the same oxidation processes control the reaction during the oxidation stages introduced above.

3.2.2 Kinetics of the Aluminum Oxidation Processes

Figure 3.1 illustrates the implementation of the processing described above. In the respective experiment spherical aluminum powder with nominal particle sizes in the range of 10 - 14 μm was heated in oxygen at 40 K/min [13]. To ensure that the heat and

mass transfer processes within the sample are insignificant, i.e., much faster than the oxidation processes of interest, the experiments were performed with different amounts of the loaded aluminum powder (10 mg and 30 mg). The resulting measured curves were identical, supporting the validity of the TGA measurements for analysis of the aluminum oxidation kinetics. There are several apparently linear regions in the plot of *Y(TGA) vs.* inverse temperature. For each such region, a straight line with the appropriate slope is shown. Comparing the data in Fig. 3.1 with the original TGA curve which is similar to that shown in Fig. 2.5, one can identify specific processes for which the activation energies can be evaluated.

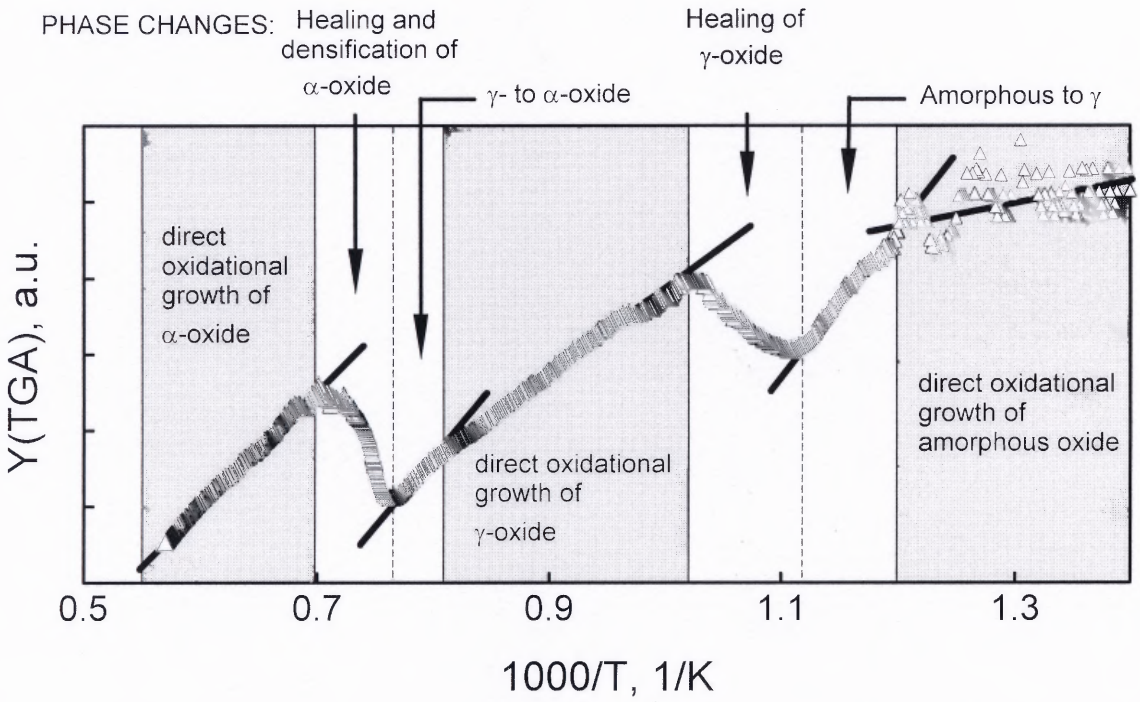

Figure 3.1 An example of a processed TGA curve used to determine the kinetic parameters of aluminum oxidation. Slopes of straight lines are proportional to the identified activation energy values.

The upper right linear portion of the curve corresponds to the growth of the natural amorphous oxide coating, or stage I in Fig. 2.5. The rate of oxidation is very small for this low-temperature process and the experimental TGA points have significant scatter. Therefore, the slope and respective activation energy are determined with a large error. At slightly higher temperatures, the processed TGA data can be described by a straight line with a much steeper positive slope, corresponding to a process with a higher respective activation energy. A positive slope, in general, illustrates an increasing oxidation rate at higher temperatures. Comparison of Fig. 3.1 and Fig. 2.5 shows that the increase in the slope of the processed TGA curve in Fig. 3.1 corresponds to the phase change from amorphous to the denser γ-oxide. This phase transformation decreases the thickness of the protective amorphous oxide layer [13]. The initially formed γ-alumina crystallites at the same time do not form a continuous surface coverage. The following portion of the processed TGA curve has a negative slope, corresponding to the decrease in the oxidation rate observed by the end of stage II, as shown in Fig. 2.5. The decreased oxidation rate is caused by "healing" of the growing γ-alumina layer, i.e. by the growth of the initial layer of γ-oxide crystallites into a continuous polycrystalline oxide scale [13]. This is accompanied by the change of the rate limiting process from the diffusion of aluminum cations in amorphous oxide to the diffusion of oxygen anions in the polycrystalline γ-oxide scale.

As the temperature continues to increase, the processed TGA data approach the next portion of a straight line with a positive slope. This part of the oxidation corresponds to the growth of the γ-oxide layer in stage III (cf. Fig. 2.5). By the end of stage III, the positive slope increases and then a region with a negative slope is observed

once again. The interpretation of these processes is analogous to that discussed above for the increase of the positive slope followed by a negative slope of the processed TGA curve in stage II. When crystallites of the denser α-oxide start forming, they initially produce little diffusion resistance to the oxygen anions. At the same time, formation of α-alumina crystallites reduces the thickness of the protective γ-alumina oxide scale. This corresponds to an increase in the slope of the processed TGA curve. As most of the γ-layer is transformed to the denser and coarser α-alumina crystallites, a continuous polycrystalline α-alumina layer is formed. The grain boundary area in this layer is smaller than that existing in the more fine-grained γ-oxide film, and the resistance of this layer to oxygen diffusion increases. As oxidation slows down after stage III, a portion of the processed TGA curve with a negative slope is observed. Continuing temperature increase results in accelerated diffusion and the final portion of the processed TGA curve with a positive slope.

Thus, five different processes described by linear portions of the processed TGA curves with positive slopes were identified and five corresponding activation energies were found. These processes are, in the order of their occurrence at increasing temperatures:

- Growth of amorphous oxide
- The amorphous to γ-alumina phase change
- Growth of γ-alumina
- The γ to α-alumina phase change
- Growth of α-alumina.

The respective activation energies were determined from a set of experiments in which spherical aluminum particles of different sizes were heated in oxygen at different rates [13]. The results of these analyses are shown in Table 3.1. Because of the significant scatter of the data points at low temperatures, the activation energy for the growth of amorphous alumina could be determined only from some of the available experiments. The activation energies shown in Table 3.1 are quite consistent for experiments conducted with different particle sizes and at different heating rates. This consistency validates the approach of processing the TGA data described above.

All described processes leading to accelerated oxidation rates at higher temperatures are considered in the oxidation model described below. The activation energies used in the model are obtained as averages from individual experiments, shown in bold in Table 3.1. Because excessive self-heating due to oxidation and corresponding perturbations of the sample temperature in experiments with the coarser 10 - 14 μm particles was less likely, these experiments were used to obtain the average activation energies for all processes in the ignition model, except for the growth of the amorphous oxide layer. This low-temperature process was better resolved in experiments with finer particles with higher specific surface; therefore the respective activation energy was obtained as the average from the individual experiments with the 3 –4.5 μm diameter particles.

Table 3.1 Activation Energies for Oxidation Stages of Aluminum.

Material	Heating Rate, β, K/min	Activation energy, E, kJ/mol				
		Amorphous phase growth	Transformation from amorphous to γ-phase	γ-phase growth	Transformation from γ- to α-phase	α-phase growth
3-4.5 μm	5	N/A[1]	344	218	361	231
	10	150	525	230	470	249
	20	106	514	233	503	254
	40	105	712	230	302	275
	Average	**120**[2]	524	228	409	252
10-14 μm	5	84	522	218	426	277
	10	N/A[1]	379	234	390	306
	20	N/A[1]	412	217	385	334
	40	104	518	239	374	308
	Average	94	**458**[2]	**227**[2]	**394**[2]	**306**[2]

[1] Experiments with low signal-to-noise ratio for the low-temperature oxidation

[2] Activation energy values used in the model of aluminum oxidation

For comparison, Table 3.2 presents the activation energies of aluminum oxidation and of phase transformations between alumina polymorphs previously reported in the literature. The activation energies found in this work for the polymorphic phase transformations, $E_{am\rightarrow\gamma}$ = 458 kJ mol^{-1} and $E_{\gamma\rightarrow\alpha}$ = 394 kJ mol^{-1}, are fairly close to the

values previously reported in the literature [64]. Previously reported activation energies for the growth of alumina layers range from 71 to about 460 kJ mol^{-1} [9, 38, 40, 65] and can generally be separated by the respective temperature ranges rather than by the type of alumina polymorph. In most investigations the polymorphic phase transformations were not taken into consideration so that the reported activation energies should be treated as compound values. Therefore, while direct comparison between the activation energies shown in Tables 3.1 and 3.2 may be of limited interest, it can be noted that the activation energies for oxidation of different alumina polymorphs found in this work are well within the range reported in the literature for both low and high heating rates. Therefore, it was hypothesized that values of activation energies detected in the low heating rate thermogravimetry experiments may be also used to describe the aluminum ignition occurring at significantly higher heating rates. Finally, as shown in Table 3.1, the following activation energies for the oxide growth regions were used in the oxidation and ignition models below: E_α = 306 kJ mol^{-1} for the growth of α-alumina; E_γ = 227 kJ mol^{-1} growth of γ-alumina; and E_{am} = 120 kJ mol^{-1} for growth of amorphous alumina.

Table 3.2 Values for the Activation Energy of Aluminum Oxidation and of Alumina Phase Transformations Reported in the Literature.

Activation Energy, KJ/mol	Reference and comment
71	[9], determined for 1600-2000 °C temperature range; the smallest activation energy reported in the literature for aluminum oxidation
418	[40], determined for 950-1300 °C range
146	[38], determined for 520-650 °C range
460	[65], grain boundary diffusion of oxygen through polycrystalline alumina
434	[64] for phase transformation from amorphous to γ-phase
502	[64] for phase transformation from γ-to α-phase

3.3 Model of Aluminum Powder Oxidation

3.3.1 Model Formulation

This oxidation model describes the formation and growth of each alumina polymorph. Because of the generic nature of these oxidation and phase transformation processes, the model is expected to describe reasonably well the oxidation of powders in a wide range of size distributions, including nanopowders. Additional corrections might need to be made in the future for extremely small size particles (e.g., < 10 nm), when the changes in the thermodynamic functions, such as enthalpy of formation, become significantly

affected by the decreasing particle size. In the model, the masses of the aluminum oxide layer and the aluminum particle core are computed as a function of time and temperature. The temperatures in this model are lower than the characteristic temperature of aluminum combustion; therefore evaporation of aluminum or its oxides was neglected. Changes in the mass of each oxide polymorph can be caused by two different processes: the mass change $\dot{m}^{ox}$ due to direct aluminum oxidation and the mass change $\dot{m}^{tr}$ due to the polymorphic phase transformations. Because of the accepted sequence of the polymorphic phase transitions: *amorphous* $\rightarrow\gamma\rightarrow\alpha$ [13], the specific masses of the amorphous, γ-, and α-oxides, referred to by the subscripts *am*, γ, and α, respectively, are described by the following differential equations:

$$\rho_{am}\dot{V}_{am} = \dot{m}^{ox}_{am} - \dot{m}^{tr}_{am\rightarrow\gamma} \tag{3.7.1}$$

$$\rho_{\gamma}\dot{V}_{\gamma} = \dot{m}^{ox}_{\gamma} + \dot{m}^{tr}_{am\rightarrow\gamma} - \dot{m}^{tr}_{\gamma\rightarrow\alpha} \tag{3.7.2}$$

$$\rho_{\alpha}\dot{V}_{\alpha} = \dot{m}^{ox}_{\alpha} + \dot{m}^{tr}_{\gamma\rightarrow\alpha} \tag{3.7.3}$$

where $\dot{V}$ is the rate of volume change, and ρ is the density. The initial volumes of both γ and α phases are equal to zero: $V'_{\gamma} = 0; V'_{\alpha} = 0$. For the amorphous oxide, the initial volume $V'_{am} = \pi/6\left(d^3_{BET} - \left(d_{BET} - 2h'_{am}\right)^3\right)$ is determined by the initial thickness of the "natural" oxide layer, h'_{am}, assumed to be equal to 2.5 nm [50-52, 66], and the particle diameter, d_{BET}, obtained from BET isotherm measurements of the powder's specific surface area [13].

The rates of mass change due to direct oxidation of aluminum are calculated from the diffusion of the rate–limiting species. As discussed above, these species are different for each oxidation stage. To simplify the boundary conditions necessary to compute the

diffusion mass flows, the model allows the direct oxidative growth of only one alumina polymorph at any given time. Specifically, only the alumina polymorph with the highest diffusion resistance is growing due to direct oxidation. Simultaneously occurring phase transformations may contribute to the growth of this or other co-existing alumina polymorphs. Further, it is assumed that the initial formation of all oxide polymorphs starts at the oxide-gas interface, i.e. the particle's outer surface. Thus, if different polymorphs coexist, the aluminum particle is surrounded by a sequence of concentric shells of the respective alumina polymorphs.

For each polymorph, the rate of direct, diffusion limited oxidation for a spherical oxide layer is described using an Arrhenius type expression (similar to Eq. (3.5)):

$$\dot{m}_i^{ox} = \frac{C_i \exp\left(-\frac{E_i}{RT_p}\right)}{\frac{1}{r_{i-1}} - \frac{1}{r_i}} \tag{3.8}$$

where C_i is the coefficient describing the diffusion of A species in different alumina polymorphs. The subscript i indicates the specific oxide polymorph, i.e., *amorphous*, γ, or α alumina. The subscript i-1 indicates the underlying substrate or "parent" material, which could be *aluminum*, *amorphous* or γ alumina, respectively. As stated above, the concentration of the rate limiting diffusing species was assumed to be zero at the reaction interface. The coefficients, C_i, were determined from the mass changes of aluminum powders measured in the TGA experiments [13] considering specific temperature ranges, for which the model predicted the existence of only one alumina polymorph. To illustrate: during the fourth oxidation stage (cf. Figs. 2.5, 3.1) only the α-oxide exists. Therefore, the equation (3.7.3) can be simplified by eliminating the term describing the

phase transformation, $\dot{m}^{tr}_{\gamma\to\alpha}$. The mass of the oxide layer is then integrated using the initial α-oxide thickness determined from the TGA curve at the beginning of stage IV. The growth of γ-oxide at the beginning of stage III, and the growth of amorphous oxide in stage I were processed similarly. Thus, processing the TGA data allowed us to determine both the activation energy and pre-exponent required to describe growth of each alumina polymorph. A detailed list of kinetic parameters used in the model is shown in Table 3.3. For the determination of the pre-exponents, the TGA experiment of 10-14 μm particles heated at 40 K/min was selected [13]. All pre-exponents were determined from this experiment.

Table 3.3 Values of the Kinetic Parameters Used in the Models for Aluminum Oxidation and Ignition.

Kinetic Parameter	Value
E_{am}	120 kJ mol^{-1}
E_{γ}	227 kJ mol^{-1}
E_{α}	306 kJ mol^{-1}
C_{am}	5.098×10^{-8} kg m^{-1} s^{-1}
C_{γ}	4.0784×10^{-3} kg m^{-1} s^{-1}
C_{α}	2.3791×10^{-2} kg m^{-1} s^{-1}
$E_{am\rightarrow\gamma}$	458 kJ mol^{-1}
$E_{\gamma\rightarrow\alpha}$	394 kJ mol^{-1}
$K_{am\rightarrow\gamma}$	1×10^{12} J mol^{-1} m^{-1}
$K_{\gamma\rightarrow\alpha}$	1×10^{8} J mol^{-1} m^{-1}
$F_{am\rightarrow\gamma}$	2×10^{15} m s^{-1}K^{-1}
$F_{\gamma\rightarrow\alpha}$	5×10^{6} m s^{-1}K^{-1}

Additional assumptions were necessary to describe the oxidation kinetics in stages II and III, when the individual γ- and α-oxide crystallites initially formed. In these periods, the oxidation rates were limited by the diffusion of aluminum cations or oxygen anions through the shrinking film of amorphous or γ-oxide, respectively. The initial diffusion resistance of the newly formed γ- and α-oxide crystallites was neglected.

However, the model needs to define the instant at which the diffusion resistance of the growing γ- and α-oxide layers becomes significant. In other words, the critical thickness of the newly formed layers of the γ- and α-oxide polymorphs needs to be identified at which these layers stop behaving as individual crystallites producing no diffusion resistance and start behaving as polycrystalline oxide scales. These transition oxide thicknesses are introduced based on literature data describing the sizes of typical individual crystallites for the γ- and α-oxides, respectively. The size of stable γ-crystallites at temperatures between 400 and 700 °C is in the 4 to 11 nm range [67], and the minimum size of stable α-crystallites is about 45 nm [68]. The minimum nucleation size of the α-crystallites formed as a result of the γ- to α-phase transformation was reported to be close to 17 nm [68]. Qualitatively, it was suggested that once the thickness of the growing alumina layer exceeds the single crystallite size, it starts behaving as a polycrystalline film with non-negligible diffusion resistance. Because of the approximate nature of this description, the "transition" thickness, h_i^m, was selected somewhat arbitrarily to be $h_\gamma^m =$ 5 nm and $h_\alpha^m =$ 30 nm, respectively. After the transition thickness of the newly formed oxide layer is achieved, the layer starts contributing to the overall diffusion resistance of the growing oxide scale. However, the initial diffusion resistance of the developing oxide layer is much smaller than the diffusion resistance of the respective regular polycrystalline film. According to the TGA results, the diffusion resistance of the newly growing oxide coverage approaches that of a regular polycrystalline layer of the γ- (or α-) oxide when the oxidation rate is slowest at the beginning of stage III (or IV, respectively.) The TGA data allow to determine the

respective oxide thickness h_i^e, where subscript i can be either γ or α, at which the oxidation starts to be described by a straight line with a positive slope, following the regions with negative slope in Fig. 3.1. The data from Ref. [13] show that the thickness h_i^e decreases at higher heating rates. Based on analysis of the available TGA data for the 10 - 14 μm size aluminum powder [13], the following empirical equation for the dependence $h_i^e(\beta)$ was obtained:

$$h_i^e = 2h_i^m + G_i \exp(-L_i\beta) \tag{3.9}$$

where $G_\gamma = 7.71$ nm; $G_\alpha =$ 116 nm; $L_\gamma =$ 1.066 s/K, and $L_\alpha = 0.439$ s/K.

For each period of oxidation during which the thickness h_i of the growing layer of the newly formed oxide polymorph i was between h_i^m and h_i^e, an effective value of the pre-exponent C_i^e was used in Eq. (3.8) instead of the coefficient C_i. The value of C_i^e was assumed to depend linearly on the oxide layer thickness:

$$C_i^e = \left[X_i - \frac{h_i - h_i^m}{h_i^e - h_i^m}(X_i - 1) \right] C_i \tag{3.10}$$

The empirical correction constants $X_\gamma =$ 200 and $X_\alpha = 150$ were selected to describe the TGA data [13] for oxidation of the 10 - 14 μm diameter particles.

3.3.2 High Heating Rates and Thin Oxide Layers

In this model, the case when the calculated thickness of the γ-oxide layer is smaller than h_γ^m corresponds to the formation of individual crystallites or, in other words, to formation of a discontinuous oxide layer with no diffusion resistance. A similar situation can occur

during the initial formation of α-alumina. In TGA experiments [13], the heating rates were low and the resulting oxide layers were relatively thick. Therefore, whenever a situation with $h_i < h_i^m$ was encountered in the aluminum oxidation model, the rate of diffusion was controlled by the parent oxide layer, i.e. amorphous or γ-oxide, for stages II and III respectively. However, for practically interesting, high heating rates, the parent oxide may disappear completely even before the layer of the new polycrystalline phase becomes continuous, that is, before the limiting thickness h_i^m is reached. In this case, a portion of the aluminum surface becomes directly exposed to the oxidizing gas environment. A similar situation has been described recently in Ref. [59] where it was suggested to use the chemical reaction kinetics to limit the oxidation rate. However, the kinetics of heterogeneous aluminum oxidation are not well known and expected to be very rapid. The model developed here describes oxidation of the aluminum surface directly exposed to the gaseous oxidizer assuming that the reaction rate is controlled by the gas phase diffusion of oxygen to the open aluminum surface. The fraction of the open aluminum surface, *f*, is introduced using the density ratio of the parent (lower density) and newly formed (higher density) oxide phases. For stage II, $f = (1 - \rho_{am}/\rho_\gamma) \approx 0.17$, where ρ_γ=3.66 g/cm^3 and ρ_{am}=3.05 g/cm^3 [44]. The concentration of oxygen at the particle surface is assumed to be zero for the diffusion rate limited oxidation. Therefore, the rate of oxidation limited by the gas phase diffusion of oxygen in stage II, $\dot{m}_{\gamma,O_2}^{ox}$, is computed considering inward Stefan flow as:

$$\dot{m}_{\gamma,O_2}^{ox} = -\ln\left(1 - \chi \frac{\mu_{O_2}}{\mu_{gas}}\right) \frac{8\pi \mu_{Al_2O_3}}{3\mu_{O_2}} \rho_{gas} D_{O_2} r_p f \tag{3.11}$$

where D_{O_2} is the coefficient of oxygen diffusion in air; r_p is particle radius, ρ_{gas} is density of gaseous environment; μ is molar mass, and the subscripts *gas*, O_2, and Al_2O_3 refer to the gaseous environment, oxygen, and alumina correspondingly; χ is the molar fraction of oxygen in the gaseous environment. Equation (3.11) is used to describe the oxidation rate during stage II instead of Eq. (3.8) until the γ-oxide thickness reaches h_γ^m. A similar description is used for the stage III oxidation when the thickness of the newly formed α-oxide is less than h_α^m while the γ-oxide layer is so thin that its diffusion resistance becomes negligible.

3.3.3 Polymorphic Phase Changes Within Alumina Layer

The rate of mass increase, $\dot{m}^{tr}_{(i-1)\to i}$, of the oxide phase *i* transformed from the oxide phase *i-1* is described as:

$$\dot{m}^{tr}_{(i-1)\to i} = 4\pi r_{i-1}^2 \rho_{i-1} v_{(i-1)\to i} \tag{3.12}$$

where v is the velocity of the interface motion. The velocity is described using a phenomenological expression, in which the thermal kinetics (similar to Ref. [64]) are supplemented by the effect of the thickness of the parent layer of transition alumina, $h_{i-1} = r_i - r_{i-1}$:

$$v_{(i-1)\to i} = F_{(i-1)\to i} T_p \left\{ 1 - \exp\left(-\frac{K_{(i-1)\to i} h_{i-1}}{RT_p} \right) \right\} \exp\left(-\frac{E_{(i-1)\to i}}{RT_p} \right) \tag{3.13}$$

The activation energies E for each specific phase transition were determined earlier by processing the TGA data. The parameters F and K describe the effect of the parent oxide thickness and were also determined by fitting the model to the experimental TGA data

[13]. The phenomenological expression Eq. (3.13) is analogous to that used in Refs. [69] and [23] to describe the phase transformations in supercooled liquids.

The rationale for introducing the effect of the oxide thickness on the speed of the phase transformation is in the intrinsic metastability of transition alumina polymorphs. Both amorphous oxide and crystalline γ-alumina are assumed to be stabilized by the interface energy [47]. With increasing oxide thickness, the stabilizing effects of the interface diminish. Literature data [46, 47] on the critical thickness of the amorphous alumina film indicate that it depends on the crystallographic orientation of aluminum substrate and varies somewhat as function of temperature. In the temperature range of 20-600 °C, this thickness is greatest for the 110 crystallographic orientation of aluminum with about 5 nm. Accordingly, the value of the parameter $K_{am\rightarrow\gamma}$ was chosen to limit the thickness of amorphous alumina at the heating rates of the TGA experiments [13]. Such limitations of the oxide thickness were only necessary at low heating rates. Similarly, the parameter $K_{\gamma\rightarrow\alpha}$ addresses the decrease of the stabilizing role of the aluminum surface with increasing thickness of γ-alumina (see Table 3.3).

3.3.4 Results and Discussion

The comparison of experimental and calculated TGA curves is shown in Fig. 3.2. Solid lines represent experimental data, and dashed lines are the calculated mass changes of the oxidizing samples.

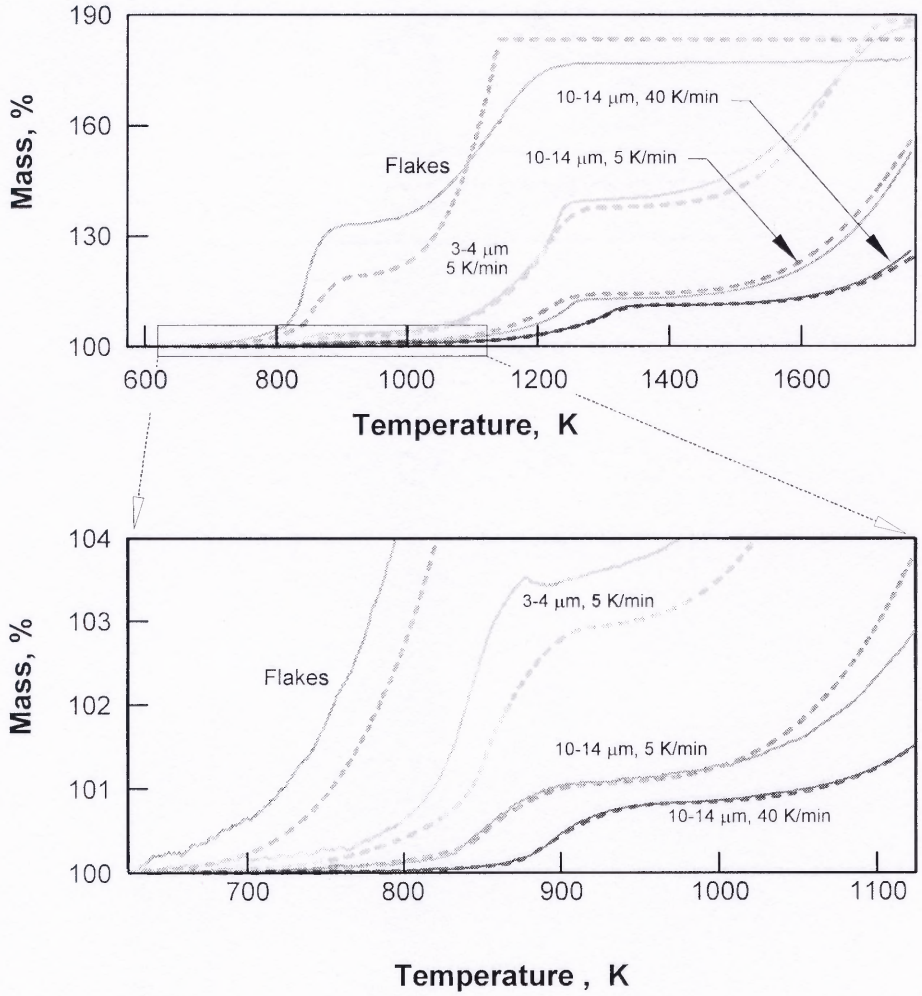

Figure 3.2 Experimental and calculated TGA curves for oxidizing aluminum samples. Solid lines represent experimental data and dashed lines show the model calculations.

In the model, one particle size was used to describe the oxidation behavior of each aluminum powder. For the spherical powders, this size was obtained from the BET measurements reported in Ref. [13]. As discussed above, the adjustable parameters used in the oxidation model (C_i, *K, and F*) were tuned to achieve the best match for the experiments with the 10 - 14 μm diameter aluminum powder oxidized at a heating rate of 40 K/min. Accordingly, the experimental and calculated curves are nearly

indistinguishable for this experiment. The two curves diverge slightly only at temperatures exceeding 1700 K, near the very end of the experimental temperature range. This nearly perfect match indicates that the five major processes accounted for in the model including direct oxidative growth of three different alumina polymorphs and two polymorphic phase transformations are adequate for the complete description of the heterogeneous oxidation of aluminum. Calculated and experimental data for the same powder at the lower heating rate of 5 K/min are also in good agreement. For the finer powder with nominal particle diameters in the range of 3 - 4.5 μm, the model prediction differs only slightly from the experimental data. This discrepancy could be due to the use of a single particle size in the model while the powder used in the experiments is actually polydisperse.

The calculations were also performed for experiments on oxidation of a flake-shaped aluminum powder [13]. Equations (3.8) and (3.12) were modified to account for the non-spherical particle shape. In equation (3.8), the difference between the inverse radii was replaced with the ratio of the oxide thickness to the flat flake surface; in equation (3.12), the particle surface was replaced with the flat flake surface. The difference between the model prediction and experimental data is more significant for the flakes than for the spherical powders. Specifically, the experimental thickness of the oxide by the end of the transformation from amorphous to γ-alumina is about two times the value predicted by the model, as reflected by the mass difference shown in Fig. 3.2 at about 900 K. This discrepancy may indicate that the thickness of the natural amorphous oxide layer was overestimated. Indeed, the commercial flake powder was produced using a ball-milling process with the addition of small amounts of an organic surface agent to

prevent agglomeration. The removal of the organic material was observed as a minor weight loss was occurring at low temperatures in the TGA experiments. This organic coating could prevent the formation of a typical, 2.5-nm thick natural oxide on the surface of flakes. Possible other sources for the discrepancy between experiment and calculation could be that the flakes' edges were not adequately accounted for as well as the effect of the crystallographic orientation and surface morphology of the aluminum flakes on the alumina phase transformations, on the orientation of the newly formed γ-crystallites, and as a result, on the rate of the grain boundary oxygen diffusion. The oxidation model also predicted a greater mass increase for the fully oxidized flake aluminum powder than was observed experimentally. Particle agglomeration and consequently incomplete oxidation in the TGA experiments could explain this observation. Addressing the above discrepancies requires detailed analysis of the reaction completeness in the TGA experiments as well as morphologies and crystallographic orientation the surfaces of different aluminum powders which was beyond the scope of the present study.

In general, it is important that the model developed here adequately describes the multi-staged oxidation for all aluminum samples studied experimentally in Ref. [13]. The oxidation model also predicts the evolution of the growing alumina film including the partial thickness of each of the present alumina polymorphs. Figure 3.3 presents the model predictions for the 10 - 14 μm diameter aluminum powder heated in oxygen at 40 K/min. The experimental TGA data were recalculated into the oxide thickness for direct comparison. Since more than one alumina polymorph can exist simultaneously, and the thickness of each sublayer is not known *a priori*, the oxide layer thickness was calculated

using the density of each individual polymorph for the purpose of this evaluation. This estimate is represented in Fig. 3.3 by the three bold lines. The shaded area represents the oxide thickness calculated according to the model developed here. Separate polymorphs are indicated by different shades of gray. The match between observation and calculation is excellent in the temperature intervals where only a single polymorph exists. In transition regions, the model prediction falls between the recalculated experimental data.

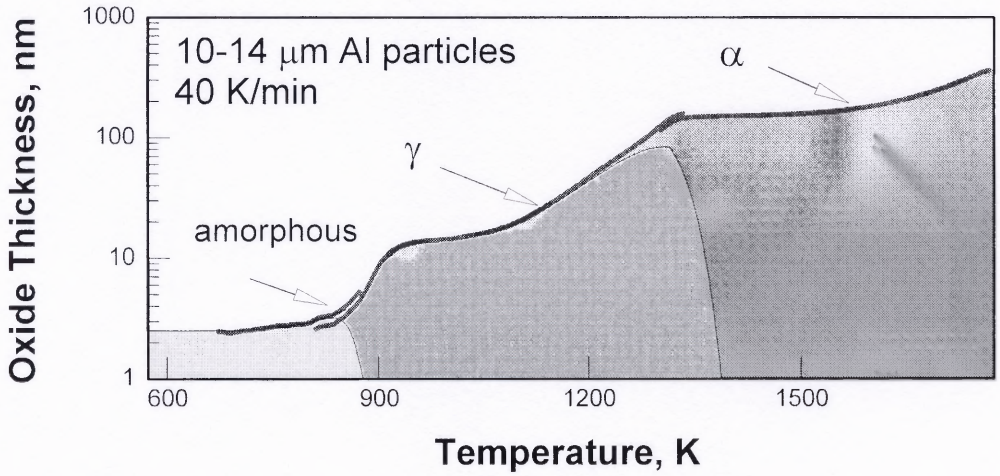

Figure 3.3 Thickness of the growing aluminum oxide layer recovered from the experimental TGA curve [13] (bold lines) and calculated thickness of different alumina polymorphs formed at different oxidation stages (represented by different shades of gray)

Following Fig. 3.3, one can clearly separate different processes occurring in the growing alumina oxide as described by the model. It is also possible to separate the periods of oxidation controlled by direct oxidative growth of different alumina polymorphs from the periods of oxidation controlled by the occurring polymorphic phase changes.

3.4 Ignition Modeling

3.4.1 Model Formulation

The model of aluminum oxidation developed in the present work allows computing the rate of heat release due to oxidation as a function of temperature and time. It is relatively easy to apply this heat release to a particle heat transfer model and to determine particle ignition based on heat transfer analysis. In this study, the ignition of a single aluminum particle inserted in hot air is described. This situation is similar to the ignition of airborne particles in the reflected shock wave near the end wall of a shock tube experiment. Particles that were initially dispersed and accelerated by an incident shock wave are effectively stopped by the reflected shock wave. Adiabatic heating causes the particles to ignite while nearly motionless [71, 72]. This simple model of heat transfer between particle and environment is selected to clearly observe the effects of polymorphic phase changes on the ignition temperature. The ignition temperature is defined here as the temperature of the environment at which an initially cold particle is observed to self-heat in excess of 2320 K, the melting point of alumina. After the oxide scale melts, the rate of aluminum oxidation is expected to increase rapidly and lead to full-fledged combustion. While gas-phase reactions dominate in aluminum combustion, only heterogeneous oxidation reactions are considered relevant for ignition in the model below.

In simplified form, the heat balance for a particle is described as:

$$c_p \, \rho_p \, V_p \, \dot{T}_p = \dot{Q}_{ph}\left(t, T_p, T_e\right) + \dot{Q}_{ch}\left(t, T_p, T_e\right) \tag{3.14}$$

where c is the temperature-dependent heat capacity, and $\dot{Q}$ is the heat transfer rate. The subscripts p and e stand for particle and environment, respectively, and subscripts ph and

ch describe physical heat transfer processes and heat generation due to chemical reaction, respectively. During melting, the particle temperature was not allowed to change.

The physical heat transfer processes covered by the term, $\dot{Q}_{ph}$, include convection and radiation:

$$\dot{Q}_{ph}\left(t,T_p,T_e\right)=\frac{\lambda Nu}{2r_p}S_p\left(T_e-T_p\right)-\varepsilon\sigma S_p\left(T_p^4-T_\infty^4\right) \tag{3.15}$$

In Eq. 3.15, λ is the thermal conductivity of the gaseous environment, Nu is the Nusselt number, S_p is the particle surface, ε is the emissivity (emissivity of oxidized aluminum surface at elevated temperatures, ε = 0.3 [73], was used in the model), and σ is the Stefan-Boltzmann constant. The subscript ∞ is used to denote the temperature of surrounding surfaces, which are assumed to be at room temperature as is the case of most shock-tube ignition experiments. In experiments where particles are ignited near the end-wall of a shock tube the particle acceleration by the incident shock is fully compensated by that generated by the reflected shock. Therefore, for simplified analysis, it is assumed that the spherical particles move slowly within the air so that Nu=2. The thermal conductivity is determined at the boundary layer temperature around the particle, T_f, calculated as: $T_f=\frac{T_e+T_p}{2}$.

The second term, $\dot{Q}_{ch}$, in Eq. (3.14) describes the oxidation processes described above in the oxidation model. It is computed as the change of the total oxide mass on the surface of an oxidizing particle multiplied by the entalphy of oxidation, H_{oxi}:

$$\dot{Q}_{ch}\left(t,T_p,T_e\right)=H_{oxi}\left(\rho_{am}\frac{dV_{am}}{dt}+\rho_\gamma\frac{dV_\gamma}{dt}+\rho_\alpha\frac{dV_\alpha}{dt}\right) \tag{3.16}$$

The enthalpies of the polymorphic phase changes in alumina are neglected.

3.4.2 Results and Discussion

As a result of multiple processes affecting the aluminum oxidation rate, the computed temperature histories of the particles inserted into the hot gas change dramatically as a function of both the particle size and the environment temperature. For a set of particle sizes, computations were carried out to determine the minimum environment temperature at which the particle would self-heat to the alumina melting point of 2320 K, and thus ignite according to the criterion introduced above. Examples of the resulting temperature histories for both ignition and non-ignition cases are shown in Fig. 3.4, 3.5, 3.6 for particles of three different sizes. Simultaneously, the processes occurring in the oxide scale are illustrated by the plots showing the overall increase in the oxide thickness and the composition of the oxide film developing in time. Note that vapor phase combustion processes are not considered in this model and therefore the predicted temperature and oxide thickness histories are only meaningful up to the melting point of alumina. Thus, calculated temperatures exceeding 2320 K are shown as dotted lines in Fig. 3.4, 3.5, 3.6 and should not be discussed.

The smallest particles with a diameter of 100 nm (*cf.* Fig. 3.4) have a relatively small heat capacity and can be heated to a temperature about 1000 K above the ambient gas as a result of rapid formation of a 5 nm thick γ-alumina surface layer. Specifically, if the ambient temperature exceeds 1310 K, self-heating results in a temperature exceeding 2320 K and consequently in ignition. The rate of oxidation and respective heat release are controlled by the gas phase diffusion of oxygen (Eq. (3.11)) to the unprotected aluminum surface formed as a result of the transition of the natural amorphous alumina into γ-alumina crystallites.

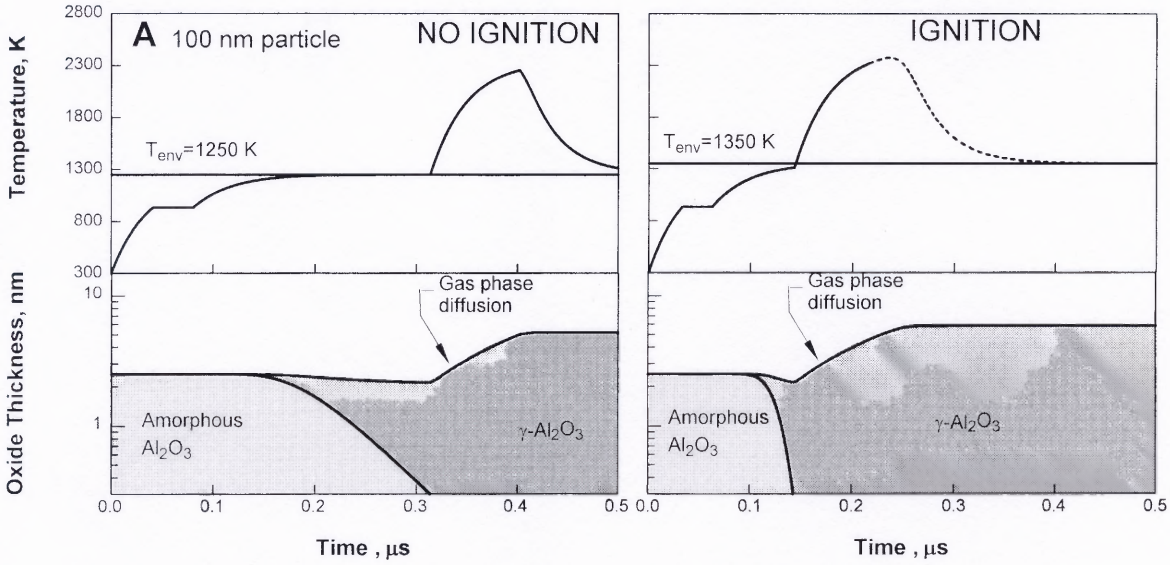

Figure 3.4 Predicted temperature histories and overall thickness and composition of the oxide layers for 100 nm aluminum particles introduced in hot air.

The ignition temperature increases for larger particles. For a particle with 500 nm diameter inserted in air at 1650 K (Fig. 3.5), the growth of amorphous oxide is extremely slow. The particle temperature increases as a result of convective heating and for a short period, as a result of rapid oxidation during the formation of a continuous γ-alumina coverage with the maximum thickness h_γ^m = 5 nm. During that short period of time, after the amorphous film disappears and the thickness of the γ-oxide remains less than h_γ^m, the oxidation rate is controlled by the gaseous oxygen diffusion to the particle surface. The temperature attained as a result of this process is close to 2000 K. The following reaction is limited by relatively slow diffusion through the continuous γ-alumina while the convective heat transfer cools the particle down preventing the ignition. However, when the environment temperature is increased to 1750 K, the rate of particle self-heating dominates over convective cooling. As shown in Fig. 3.5, at about

1.5 μs the 500 nm particle becomes hotter than the surrounding gas, but the self-heating continues, eventually resulting in ignition. The ignition model initially predicts the particle self-heating controlled by gas phase oxygen diffusion (up to about 1.7 μs) followed by self-heating limited by the diffusion of oxygen in the newly formed γ-alumina scale; the latter process (described by Eq.(3.8) with the preexponent C_γ replaced with C_γ^e from Eq. (3.10)) results in the particle ignition.

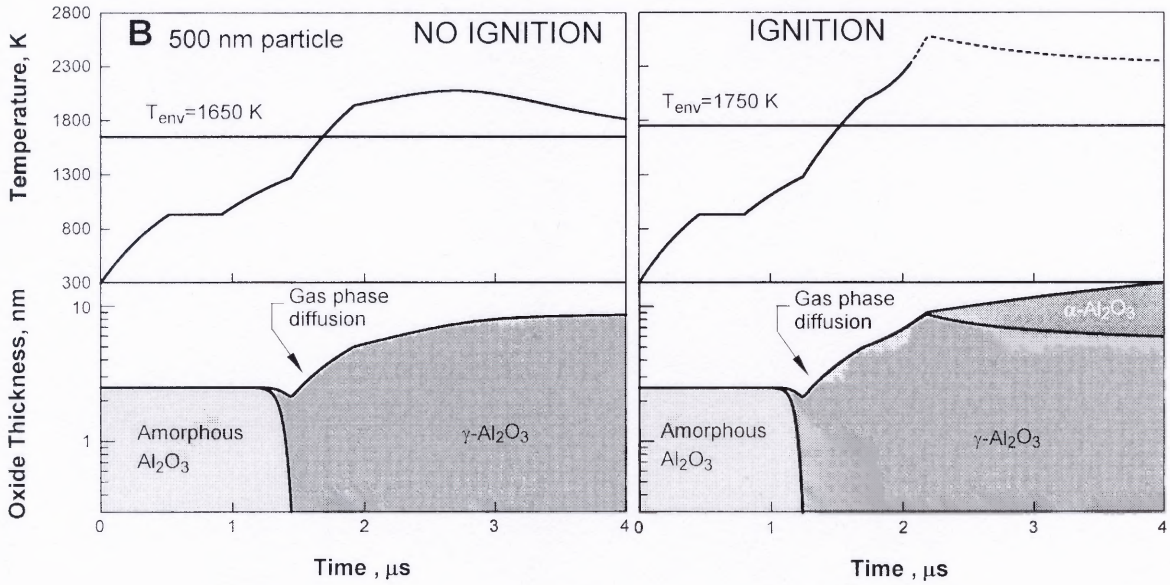

Figure 3.5 Predicted temperature histories and overall thickness and composition of the oxide layers for 500 nm aluminum particles introduced in hot air.

For still larger particles with 5 μm diameter, self-heating as a result of gas phase diffusion of oxygen to the unprotected aluminum surface formed as a result of the amorphous-to-γ transition is insufficient to cause ignition, as shown in Fig. 3.6. By the time the thickness of the γ-oxide reaches h_γ^m = 5 nm, the particle temperature is still fairly low and convective particle heating continues. For the 5 μm diameter particle in

air at 1900 K, the heterogeneous oxidation does not lead to ignition. However, at a higher environment temperature, the processes of heterogeneous oxidation become sufficiently fast to cause ignition. For air at 2100 K, the ignition model initially predicts the particle self-heating limited by diffusion of oxygen in γ-alumina (up to about 300 μs) followed by self-heating limited by the gas phase diffusion of oxygen to the open Al surface produced as a result of γ→α-alumina transformation (from about 300 to 330 μs), eventually leading to ignition. The latter process is described by the modified Eq. (11) where the fraction of open aluminum surface, f, reflects the ongoing alumina phase transformation from γ to a denser α phase: $f = (1 - \rho_\gamma / \rho_\alpha) \approx 0.083$, where ρ_α = 3.99 g/cm^3 [44].

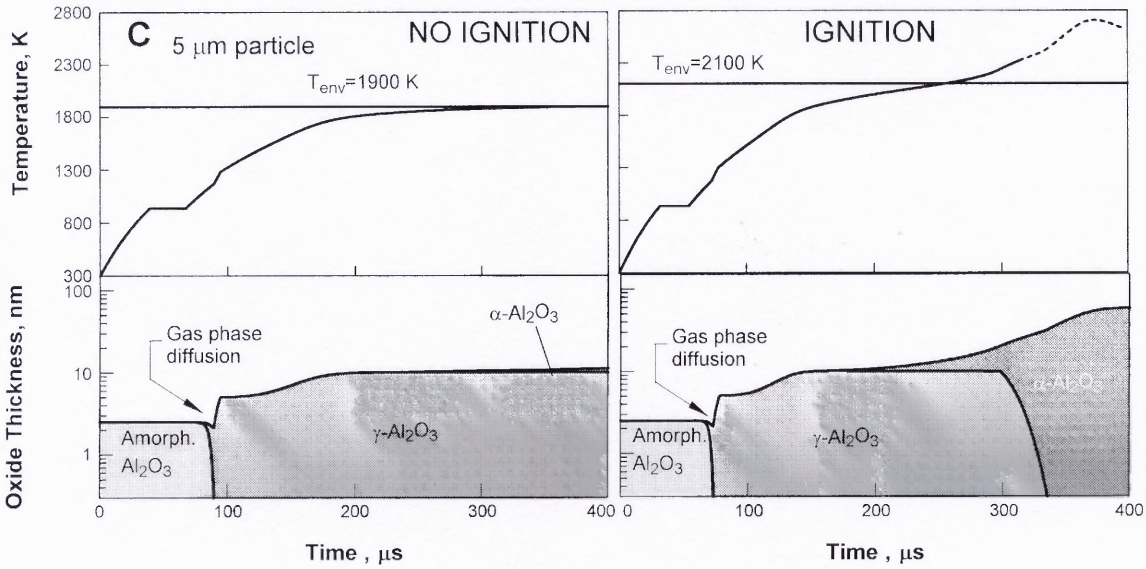

Figure 3.6 Predicted temperature histories and overall thickness and composition of the oxide layers for 5 μm aluminum particles introduced in hot air.

The results of similar calculations, showing only the minimum environment temperature at which ignition is observed for particles of different sizes are shown in Fig. 3.7.

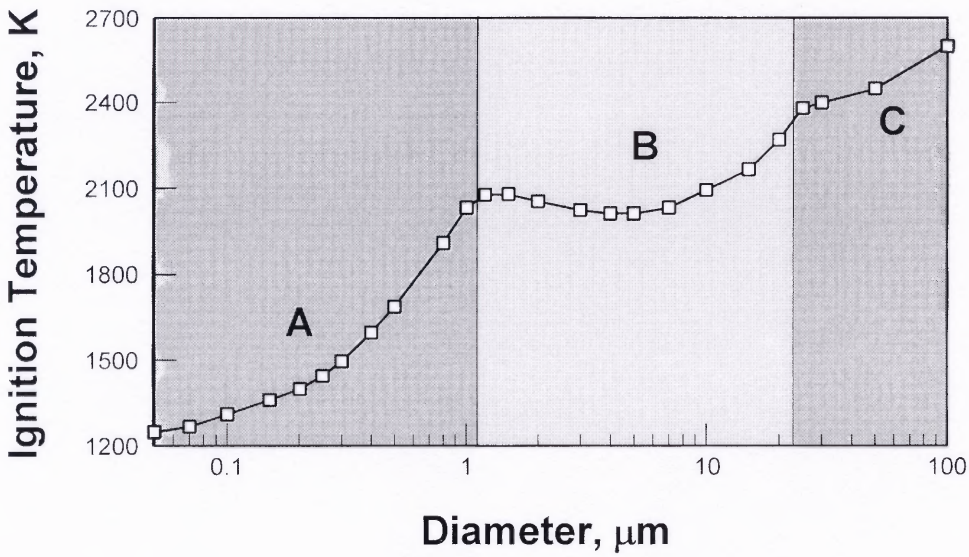

Figure 3.7 The minimum air temperature at which ignition is predicted to occur for aluminum particles of different sizes.

Three different processes which can result in particle heating to 2320 K were identified for particles of different sizes. Particles smaller than 1.2 μm (labeled in Fig. 3.7 as zone *A*) ignite at very low temperatures, when the continuity of the amorphous oxide layer is disrupted as a result of the formation of γ-alumina. The oxidation process leading to ignition of these small particles is controlled by the gas phase diffusion of oxygen or by oxygen diffusion through the thin layer of γ-alumina.

Particles with sizes in the range from 1.2 μm to about 25 μm (labeled as zone *B* in Fig. 3.7) ignite due to oxidation controlled by the processes associated with formation of α-alumina. For these particles (similar to the 5 μm case illustrated in Fig. 3.6), the rate of exothermic oxidation leading to ignition is initially limited by the grain boundary

diffusion of oxygen in γ-alumina. Later in the self-heating process, when the particle temperature becomes relatively high, the γ→α-alumina phase change occurs and the rapid oxidation continues as a result of the gaseous oxygen diffusion to the open Al surface eventually leading to ignition. For particles in the 6 to 25 μm size range, the openings in the newly produced α-oxide layer disappear before the particles ignite. However, when the environment temperature is sufficiently high the particle self-heating ultimately leading to ignition continues as a result of the oxygen diffusion through the growing layer of α-alumina.

According to the model, for aluminum particles greater than about 25 μm diameter (the size range labeled *C* in Fig. 3.7), the self-heating does not lead to ignition. Therefore, those particles can only be ignited at environment temperatures higher than 2320 K.

The model predicts a significant effect of the aluminum particle size on its ignition temperature, which is generally supported by the experimental data available in the literature, e.g., [5, 6, 9-20]. Indeed, reported ignition temperatures vary from about 1000 K for submicron sized particles [11-13, 20] to the alumina melting temperature of about 2300 K for particles larger than 100 μm [14, 15, 18, 19]. For particles with sizes in the 1-100 μm range, the experimental data vary widely and essentially fill the entire range of temperatures from 1000 to 2300 K [5-6, 9, 11, 16, 17, 20]. The significant advantage of the model developed here is that these very diverse ignition temperatures are predicted within a self-consistent description of the processes of aluminum oxidation for particles of different sizes.

As shown in Fig. 3.7, the lowest ignition temperatures predicted by the model are still somewhat higher than 1000 K, reported in the literature for some aluminum nanopowders. However, the model has only considered the energy balance for a single particle, while the convective heat losses decrease dramatically for particle agglomerates or clouds that are often used in experiments. For a simple estimate, one may neglect the convective heat removal altogether and consider to what temperature can agglomerated particles self-heat while the natural amorphous oxide layer grows and transforms into a continuous polycrystalline γ-alumina coverage. If the final temperature of such an ensemble exceeds 2320 K, it can be considered igniting. The ignition temperature estimated in such a way is a function of the initial oxide thickness and size of the individual particles. Estimates showing the minimum environment temperature at which ignition of agglomerated aluminum particles can be expected are shown in Fig. 3.8 for three selected particle sizes and for a range of initial (natural) oxide thicknesses. The natural oxide thickness for nano-particles is reported to be in the 2 to 3 nm range, e.g. [11, 66], similar to that for micron-size particles. However, in some reports the initial oxide thickness ranges from 0.5 [47] to about 4 nm [49], justifying the range of natural oxide thicknesses used in the estimates shown in Fig. 3.8. These estimates illustrate the potential ignitability of nano-size aluminum particle agglomerates and illustrate the feasibility of experimentally observed ignition temperatures lower than expected for single particles, as shown in Fig. 3.7. Another interesting result of this simple estimate is that when very fine particles (e.g., 50 nm diameter) are agglomerated, they could be pyrophoric even if they are covered with a 2.5 nm- thick natural oxide layer.

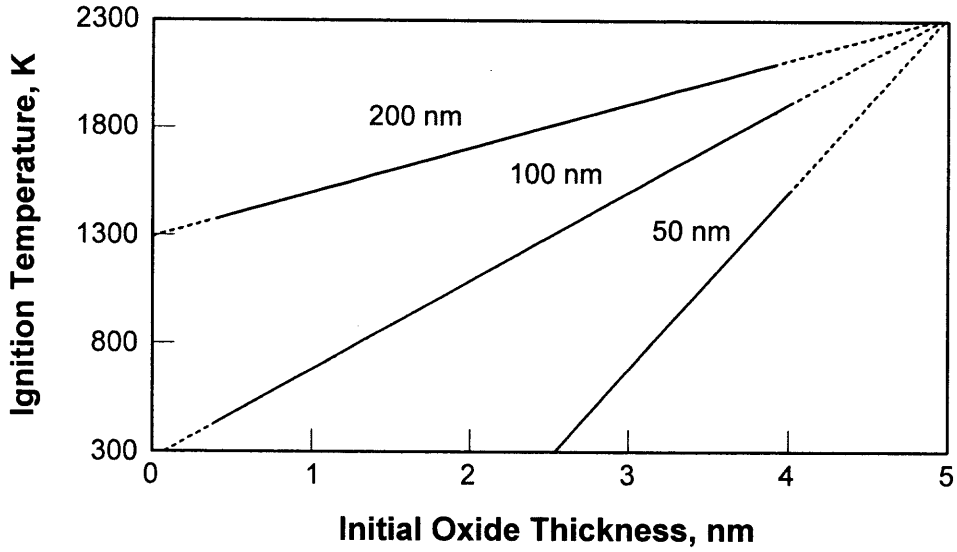

Figure 3.8 Estimated ignition temperatures of agglomerated aluminum nanoparticles as a function of the initial thickness of aluminum oxide film.

3.5 Conclusion

The aluminum oxidation mechanism is quantified and used to develop a simplified model of aluminum particle ignition. Thermogravimetric data [13] for oxidizing aluminum powders are used to obtain kinetic parameters for both growth and phase transformations in the oxide layer.

A new methodology is developed for the interpretation of TGA experiments and the recovery of oxidation kinetics. Assuming that the oxidized aluminum particles are spherical, the sample mass history is transferred into alumina thickness history. Oxidation kinetics are determined assuming that reaction rates are controlled by diffusion through the growing alumina scale. This approach enables one to account for multiple and partially overlapping oxidation processes, unlike traditional isoconversion methods.

The stepwise oxidation of aluminum observed in the TGA experiments was described quantitatively for different particle sizes and heating rates.

An aluminum ignition model has been developed for single aluminum particles inserted in a hot oxygenated gas. The model accounts for concurrent processes of the growth and phase transformations occurring in the oxide scale. Additional assumptions are made about the oxidation rate when the continuity of the nanometer-thick oxide layer is disrupted because of significant volume changes due to polymorphic phase transformations. Specifically, it is assumed that alumina crystallites with increasingly higher densities form as a result of polymorphic phase changes in very thin oxide scales, which leads to discontinuities in the oxide layer and exposes parts of aluminum surface to atmospheric oxygen. In such cases, the oxidation rate becomes limited by the diffusion of gaseous oxygen until the openings heal. The kinetic relations of the polymorphic phase changes used in the model were determined from TGA experiments. Based on heat transfer analysis, particles of different sizes are predicted to ignite as a result of self-heating during different oxidation stages involving the formation of different oxide polymorphs. The proposed model of aluminum ignition predicts a significant effect of the particle size on the ignition temperature, consistent with experimental data available in the literature.

The range of ignition temperatures is distinctly different for nanopowders, particles in the 1 - 10 μm size range, and coarser particles. Generally, finer particles ignite at lower temperatures.

CHAPTER 4

OXIDATION AND MELTING ALUMINUM NANOPOPWDERS

4.1 Introduction

Nanosized aluminum powders have been produced and evaluated as reactive additives to propellants and explosives [57, 74-75] as well as components of nanocomposite energetic materials [76, 77]. An accelerated reaction rate is generally due to an increase in the specific surface of the powder. It has also been suggested that the melting point depression reported to occur for metal nanoparticles [78-83] could result in an earlier aluminum ignition (triggered by accelerated oxidation) and therefore, in shorter ignition delays [84, 85]. However, experimental data on melting of aluminum nanoparticles are scarce and it was recently shown that no correlation exists between melting and ignition or oxidation for micron-sized aluminum powders [13, 60]. The main objectives of this work are to characterize experimentally melting and oxidation of the nano-sized aluminum powders. The effect of the particle sizes on melting and oxidation kinetics was specifically addressed. Instead of a common practice of representing each powder sample with a single average particle size, the experimental size distributions for different nanopowders were obtained and used directly for quantitative interpretations of the measurements.

4.2 Experimental

4.2.1 Particle Size Distributions

Three aluminum nanopowders with the respective BET particle sizes of 44, 80, and 121 nm were provided by Nanotechnologies Inc., Austin, TX. For each "as received" powder, the particle size distributions (PSD) were determined using small angle x-ray scattering (SAXS). To achieve a reasonable fit with the SAXS measurements, the size distribution for each powder was represented by a linear superposition of two log-normal distributions.

Specific parameters determined from the SAXS measurements describing the PSD are presented in Table 4.1. The frequency function, *P(D)*, of aluminum nano-particle distributions that was used in the study to describe melting and oxidation of aluminum nano-powders, is expressed as:

$$P(D)=\sum_{k=1}^{2} W_k \frac{1}{D\ln(\sigma_k)\sqrt{2\pi}} \exp\left(-\frac{\left(\ln(D)-\ln\left(\langle D\rangle_k\right)\right)^2}{2\ln^2(\sigma_k)}\right) \qquad (4.1)$$

where D is the diameter of the aluminum core, which is a parameter measured by SAXS directly, the index k represents two log-normal distributions, W_k is a weight factor for each of those log-normal distributions, σ_k are the geometric standard deviations, and $\langle D\rangle_k$ are the geometric mean diameters. The aluminum powder manufacturers report the oxide layer thickness, h_{ox}, in the range of 1.8-3.5 nm [86]. It was assumed that "as received" powders had an oxide thickness of 1.8 nm, so that the particle diameters measured by SAXS and representing the metal core were corrected accordingly. Powders stored in the laboratory for the duration of this project (about 6 months)

continued to slowly oxidize as was determined from the thermo-gravimetric measurements performed over this period of time with the same powder batches. This growth of oxide thickness and respective changes in the overall particle diameters were accounted for while interpreting the oxidation measurements as described below.

Table 4.1 Particle Size Distributions of the Al Nanopowders Obtained From SAXS.

BET particle size, μm (powder ID)	Log-normal distribution parameters and weight factors		
	Geometric mean diameter, $<D>$, nm	Geometric standard deviation, σ, nm	Weight factor
44	18.8	1.80	0.99942
	129.2	1.71	0.00058
80	33.4	1.75	0.999936
	328	1.47	0.000064
121	38.4	1.72	0.997937
	196.6	1.48	0.002603

The volume-based distributions for the aluminum core diameters, as determined by SAXS and described by Eq (4.1) and in Table 4.1, are presented in Figure 4.1. PSD for each powder is skewed to the right side due to the presence of relatively large particles represented by the second lognormal mode (see Table 4.1). These large particles produce a noticeable contribution while such volumetric processes as melting and oxidation are considered.

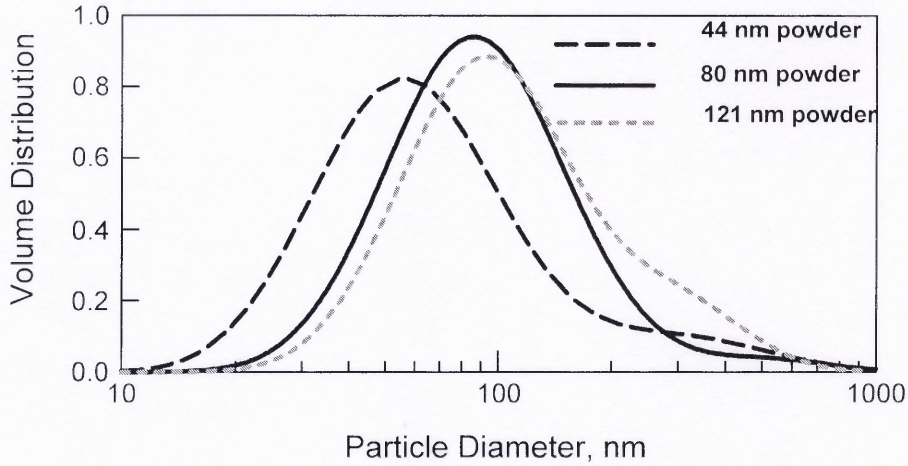

Figure 4.1 Volume based PSD for different aluminum nano-powders. Vertical axis shows percent of a differential of cumulative volume distribution for aluminum core divided by the logarithm of the particle size. Therefore, the area under each normalized PSD curves equals to 100%.

4.2.2 Thermal Analysis Experiments

Melting and oxidation of the powders were studied using a Netzsch Simultaneous Thermal Analyzer STA409 PC. The instrument was calibrated for temperature with the melting points of a set of metal standards resulting in a temperature accuracy of ±1 °C.

To describe melting, differential scanning calorimetry (DSC) was performed in argon, heating powders up to 750 °C with a rate of 5 °C /min. The 35 – 45 mg samples were heated in alumina and platinum sample holders. To establish reproducible initial conditions for the DSC measurements, each sample was heated from room temperature to 300 °C at 20 °C /min and kept at 300 °C for about 30 minutes, prior to the main heating program. During heating and melting, sintering can occur, affecting the powder sample's geometry, location in the DSC sample holder, and the heat transfer in the DSC measuring head. To minimize such artifacts, three experiments were performed. In the first

experiment, the powder was loosely packed in the sample holder. In the second test, the powder was pressed into a pellet. Finally, in the third experiment, the powder was mixed with alumina powder (Inframat Advanced Materials LLC, Farmington, CT, particle size ≈150 nm) in the 1:1 mass ratio and the mixture was loosely packed in the sample holder. The results of all three types of experiments were generally consistent, while the most reproducible measurements were obtained with the mixed Al/Al_2O_3 powders. These measurements are presented below.

Oxidation was characterized using thermo-gravimetric analysis. Samples of 25 - 40 mg contained in alumina crucibles were heated in an oxygen/argon environment (oxygen flow rate 10 ml/min, argon flow rate 50 ml/min) from room temperature to 1350 °C. Heating to higher temperatures, performed in a limited number of experiments, did not result in any further weight increase. Two heating rates of 1 and 5 °C /min were used in the study.

4.3 Oxidation Modeling

Recently, oxidation of aluminum powders was described considering formation of different polymorphs of Al_2O_3 [13, 61]. The same model, described in detail in the chapter 3 and Ref. [61], was modified in this work to reflect the effect of particle size on the diffusion rate, which is only significant for nanopowders. After this modification, the model was used to predict the TGA curves expected for each powder sample while the PSD for each powder was obtained from SAXS measurements. All particles were assumed to be spherical.

4.3.1 Major Processes During Aluminum Oxidation

A detailed discussion of major processes occurring during oxidation of aluminum powders is given in the chapter 3. The following abbreviated discussion is given for a self-containing description of the modified oxidation model.

Aluminum particles are covered by a thin layer of "natural" amorphous oxide. At low temperatures, the thickness of the amorphous oxide increases. At elevated temperatures, the amorphous alumina transforms into a denser γ-Al_2O_3 polymorph. This phase transformation can reduce the thickness of the oxide layer. For thin oxide layers observed at high heating rates, this phase change can also result in local discontinuities in the oxide coverage [13, 61]. Thus, the rate of oxidation accelerates rapidly until a continuous, polycrystalline layer of the γ-Al_2O_3 is produced. As the temperature continues increasing, the layer of the γ-Al_2O_3 grows until crystallites of an even denser α-oxide start forming. Formation of a higher density oxide polymorph once again results in a reduction in the overall oxide thickness and accelerated oxidation continuing until the entire oxide layer transforms into a continuous, polycrystalline α-Al_2O_3 film. According to this model [13, 61], five processes need to be analyzed to describe the oxidation quantitatively. These processes are, in the order of their occurrence at the increasing temperatures:

- Growth of amorphous oxide
- The amorphous to γ-alumina phase change
- Growth of γ-alumina
- The γ to α-alumina phase change
- Growth of α-alumina.

4.3.2 General Model Formulation

The mass of each alumina polymorph and the mass of metallic aluminum are computed as a function of time and temperature. To account for the effect of specific PSD, the computations are made for each particle size and then integrated over the PSD. According to the model, changes in the mass of each oxide polymorph can be caused by two different processes: a mass change $\dot{m}^{ox}$ due to the direct aluminum oxidation and a mass change $\dot{m}^{tr}$ due to polymorphic phase transformations. Because of the accepted sequence of the polymorphic phase transitions: *amorphous* $\rightarrow\gamma\rightarrow\alpha$ [13], the rates of relative mass changes for aluminum core and for corresponding shells of the amorphous, γ-, and α-oxides, referred to by the subscripts *Al, am*, γ, and α, respectively, are determined for each instant of time (or for each temperature) from the following equations:

$$\rho_{am}\dot{V}^{rel}_{am} = \int\left[\dot{m}^{ox}_{am} - \dot{m}^{tr}_{am\rightarrow\gamma}\right]P(D)\,dD \tag{4.2.1}$$

$$\rho_{\gamma}\dot{V}^{rel}_{\gamma} = \int\left[\dot{m}^{ox}_{\gamma} + \dot{m}^{tr}_{am\rightarrow\gamma} - \dot{m}^{tr}_{\gamma\rightarrow\alpha}\right]P(D)\,dD \tag{4.2.2.}$$

$$\rho_{\alpha}\dot{V}^{rel}_{\alpha} = \int\left[\dot{m}^{ox}_{\alpha} + \dot{m}^{tr}_{\gamma\rightarrow\alpha}\right]P(D)\,dD \tag{4.2.3.}$$

$$\rho_{Al}\dot{V}^{rel}_{Al} = -\frac{2\mu_{Al}}{\mu_{Al_2O_3}}\int\left[\dot{m}^{ox}_{am} + \dot{m}^{ox}_{\gamma} + \dot{m}^{ox}_{\alpha}\right]P(D)\,dD \tag{4.2.4}$$

where $\dot{V}^{rel}$ is rate of relative volume change. All the variables are functions of time, and all variables inside the square brackets are functions of the initial diameter of the particle aluminum core, *D*. The temperature of aluminum particles affecting the rates of mass change, $\dot{m}^{ox}_{i}$ and $\dot{m}^{tr}_{(i-1)\rightarrow i}$, increases from room temperature at a constant rate used in the

oxidation TGA experiments. The modeled TGA weight change was calculated by integrating equations (4.2.1-4.2.4) numerically.

The rates of mass change due to direct oxidation were described by the model of diffusion for the rate–limiting species. To simplify the boundary conditions necessary to compute the diffusion mass flows, the model allows the direct oxidative growth of only one alumina polymorph at any given time. Specifically, at any given time only the alumina polymorph with the highest diffusion resistance, which is tracked during the calculations, is allowed to grow due to the direct oxidation. The phase transformations can occur simultaneously and may contribute to the growth of any co-existing alumina polymorph. Thus, if several alumina polymorphs coexist, each particle is surrounded by concentric shells of the respective oxide polymorphs. The spherical symmetry allows one to recalculate volumes of alumina and aluminum core (and radii of corresponding shells, r_i) for each specific initial particle size by integrating over time equations (4.2.1-4.2.4) written in the differential form, i.e., for a given particle diameter rather than integrated over PSD.

4.3.3 Diffusion Limited Oxidation

For each polymorph, the rate of direct, diffusion limited oxidation for a spherical oxide layer of outer radius, r_i, is described by the same Arrhenius type expression (see Eq. (3.8)) as was used before for the oxidation modeling of micron sized particles. The values of parameters C_i, and E_i, were also the same as determined recently for the oxidation of micron-sized aluminum particles (see Table 3.3).

4.3.4 Diffusion in Thin Oxide Layers

Additional assumptions were necessary to describe the oxidation kinetics when the oxide thickness was comparable to the size of individual γ- and α-oxide crystallites. When such crystallites are initially formed, the discontinuities in the oxide coverage are produced [13, 61]. The initial diffusion resistance of the newly formed γ- and α-oxide crystallites was neglected. A critical thickness for each of the new growing layers of the γ- and α-oxide polymorphs was identified at which these layers stop behaving as individual crystallites and start producing diffusion resistance typical of respective continuous polycrystalline layers. These transition oxide thicknesses, introduced previously to describe oxidation of the micron sized aluminum powders [61], were also used here. According to the model proposed in Ref. [61] and described in details in the chapter 3 the diffusion resistance of a new growing oxide layer increases linearly with the increase in the oxide thickness until a continuous, polycrystalline oxide coverage is formed.

4.3.5 Polymorphic Phase Changes in Al_2O_3

The rate of mass increase, $\dot{m}^{tr}_{(i-1)\to i}$, of the oxide phase *i* transformed from the oxide phase *i-1* is described using the expressions introduced in chapter 3 (Eqs. (3.12) and (3.13)). The activation energies *E* for each specific phase transition, as well as, parameters *F* and *K* were determined earlier by processing the TGA data for the micron sized particle (see chapter 3 and Ref. [61]).

4.3.6 Initial Conditions

The initial volumes (and thus thicknesses) of both γ and α phases were equal to zero. The initial volumes of the amorphous oxide and aluminum core were considered as a function of PSD using the SAXS measurements and a size-dependent correction required to account for "aging" or oxidation of the powders stored in the laboratory. The overall mass of the initial oxide for the "aged" particles was determined from the total mass increase measured from the respective TGA curves acquired in the oxygen/argon environment. Thus, a specific correction was introduced for interpretation of each specific TGA experiment. The oxidation of powders during their storage was analyzed assuming a uniform, 1.8 nm, initial oxide thickness for "as received" particles of all sizes and using equations (4.2.1), (4.2.4), and (3.8) while allowing the particle's temperature to remain at a constant, room temperature level. The growing thickness of the amorphous oxide layer was computed as a function of time until the total mass of the oxide layer matched the oxide mass inferred from the TGA measurements. An example of the resulting distribution of the oxide thickness over the particle diameter is shown in Fig. 4.2.

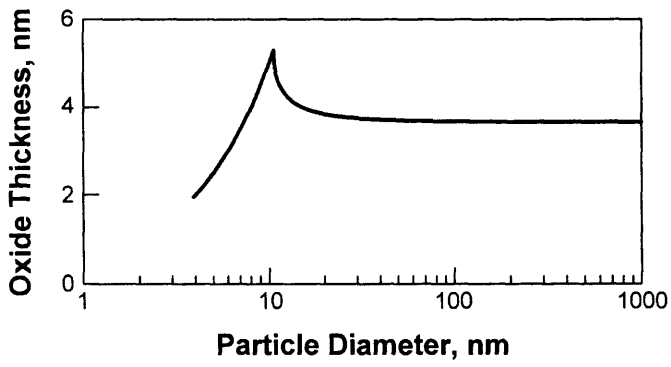

Figure 4.2 Calculated initial thickness of the amorphous oxide layer as a function of the particle size for an aluminum nanopowder (BET diameter 80 nm) stored in the laboratory for a period of time.

The calculations in which the diffusion rates depend on particle size (*cf.* Eq. (3.8)) predict that the oxide thickness increases faster for the finer particles. Thus, the left, rising part of the curve in Fig. 4.3 corresponds to the finer particles that are fully oxidized. For such particles the oxide thickness equals to the particle radius. For larger particles, oxide thickness decreases as the particle size increases. It is clear that the size-dependent "aging" effect is substantial only for the particles that are smaller than 20 nm while it can be neglected for coarser particles.

4.4 Melting Models

4.4.1 Melting Temperature and Entropy Dependence on Particle Size

The effect of particle size on its melting temperature and latent heat of melting for nano-sized metal particles has been extensively discussed in the literature. A model commonly quoted in recent papers dealing with aluminum nanopowders used in energetic materials, e.g. [85], was developed about five decades ago [78]. That model describes the melting point, T_m, as a function of the particle diameter, d_p , and the oxide shell thickness h_{ox}, as:

$$T_m = T_b \left[1 - \frac{4\sigma_{sl}}{H_b \rho_{Al} \left(d_p - 2h_{ox} \right)} \right] \tag{4.3}$$

where T_b is the melting temperature of bulk aluminum, H_b is the enthalpy of fusion of bulk aluminum, and σ_{sl} is the interfacial surface tension between the solid and the liquid. The difference in the molar volumes between solid and liquid aluminum was neglected.

More recently, a theoretical model of melting for nanocrystalline metal powder was developed by Jiang et al., [80-82]. It has been proposed that the melting point

depends on the diameter of aluminum nano-crystals, assumed in our study to be equal to the diameter of particle aluminum core, as:

$$T_m = T_b \exp\left(-\frac{2H_b}{3RT_b} \frac{1}{\left(D/6l - 1 \right)} \right) \tag{4.4}$$

where, and l is the length of the Al-Al atomic bond. Furthermore, it was suggested that for nanoparticles, the latent heat of melting, H_m, depends on the particle diameter according to:

$$H_m = H_b \exp\left(-\frac{2H_b}{3RT_b} \frac{1}{D/6l - 1} \right) \left[1 - \frac{1}{D/6l - 1} \right] \tag{4.5}$$

Finally, processing the experimental results reported by Eckert et al., [83] suggests phenomenological dependencies for both the melting point and latent heat of melting as functions of the aluminum core diameter (expressed in nanometers):

$$T_m = 977.4 - \frac{1920}{D} \tag{4.6}$$

$$H_m = 14.705 - \frac{177.49}{D} \tag{4.7}$$

The experimental data presented in Ref. [83] limit applicability of the trends given by Eqs. (4.6, 4.7) for the particles with diameters in the range of 12.07 nm < D < 43.24 nm. For larger particles, T_m=T_b and H_m=H_b. For particles with the metal core smaller than 12.07 nm, the latent heat of melting is reported to be negligible [83].

4.4.2 Modeling of Experimental DSC Signal

Three different melting models introduced above were used together with the experimental PSD to quantitatively predict the DSC signals expected while different powder samples melt. Each calculation was compared to a specific DSC run. The correction for the initial oxide thickness as a result of aging for each specific DSC run was made in the respective calculations using the procedure described above and the results of the concurrent TGA measurements. Equations (4.3), (4.4), and (4.6) represent functional dependence of the melting temperature on the particle diameter. Each of these equations was converted into a respective dependence of the aluminum core diameter as a function of the melting temperature, $D = D(T_m)$. The converted functional dependencies and their temperature derivatives $\frac{dD}{dT}$ were used to predict the DSC signal directly. The DSC experiments were performed at a constant heating rate, β, so that the DSC signal, $\dot{Q}_{DSC}$, detected at each specific temperature, T, was calculated as:

$$\dot{Q}_{DSC} = M_s \; P(D) \; \frac{\pi}{6} D^3 \, H_m \; \frac{dD}{dT} \, \beta \tag{4.8}$$

where M_s is the parameter accounting for frequency function normalization and proportional to the mass of the aluminum metal in the analyzed nanopowder sample.

4.5 Results and Discussion

Experimental DSC curves showing the melting endotherms for different powders are shown in Fig. 4.3 together with the TGA curves showing the weight increase for the same powders as a result of oxidation.

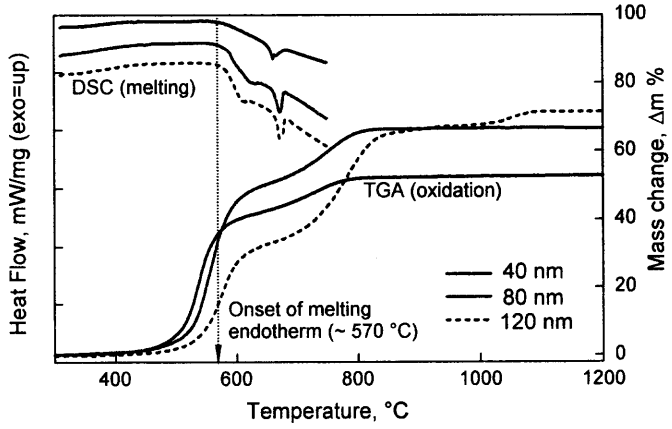

Figure 4.3 DSC and TGA curves measured for three aluminum nanopowders in argon and oxygen, respectively. Both sets of curves were acquired at a heating rate of 5 °C/min.

For all powders, the oxidation is observed to begin at the temperatures substantially lower than the onset for the melting endotherm (occurring at around 570 °C for all powders). Thus, no correlation between melting and oxidation is observed, similarly to the results for the micron-sized Al powders [13, 60, 61]. The substantial difference in the slopes of the DSC curves before and after melting is most likely explained by the change in the powder morphology as a result of its melting. The change in morphology affects the heat transfer within the DSC sample holder and, therefore, the baseline of the measurement.

Comparisons of the experimental TGA curves with the curves predicted by the recently developed aluminum oxidation model are shown in Fig. 4.4. The absolute measured mass increase becomes smaller for the same particles used in different experiments after increasingly longer storage periods, indicating that oxidation did occur during the storage. At the same time, the final mass increases for the calculated and experimental TGA curves always coincide because of the discussed above correction for

the initial oxide layers for the powders stored in the laboratory during different periods of time. The calculations, in general, reproduce well the shapes of the experimental TGA curves. The shift between the TGA curves as a function of the heating rate is also well described.

There are, however, minor but systematic discrepancies between the predicted and calculated curves, as shown in Fig. 4.4. The calculated TGA curves are extremely sensitive to the specific shape of the particle size distribution and particle surface morphology. It is suggested that the disagreement between the presented oxidation theory and experiments is within the ranges expected based on the accuracy with which the particle size distributions are determined.

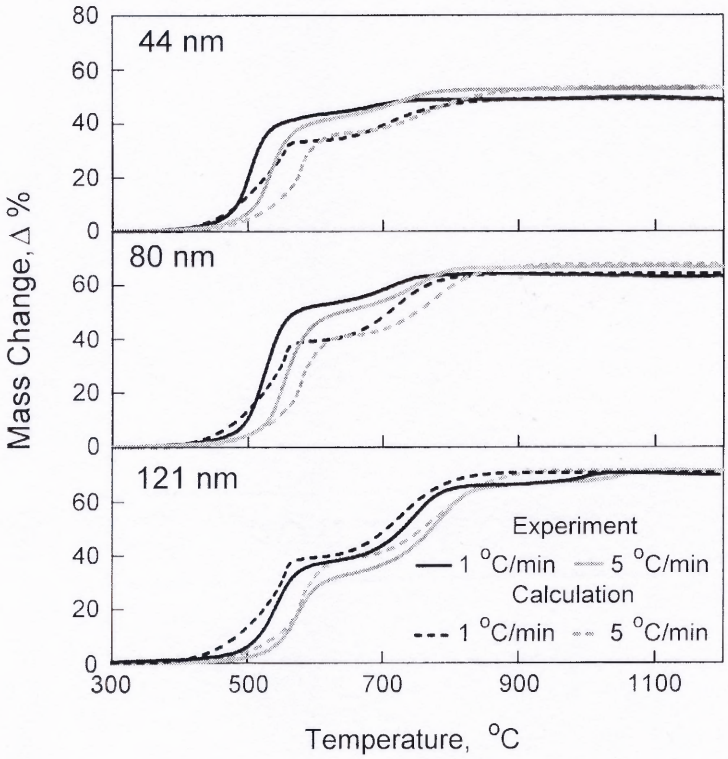

Figure 4.4 Comparison of experimental TGA curves with results of the oxidation modeling.

Comparisons of the experimental DSC melting curves with the curves predicted to describe respective measurements by different melting models of metal nanopowders are presented in Fig. 4.5. No close agreement between experiment and any of the tested melting models was observed; however, the overall shape of the melting endotherm was predicted by all the models. In particular, it is interesting that the experimental endotherms have at least two peaks and this overall shape is generally predicted considering the bimodal size distributions obtained from SAXS (see Table 4.1). Note that according to Eqs. (4.6, 4.7) [83], only a fraction of the powder is predicted to melt before T_b = 660 °C is reached. The rest of the powder, as noted in Fig. 4.5, is expected to melt at a constant temperature of T_b, so that respective calculations for the melting endotherms could not be performed and are not shown in Fig. 4.5.

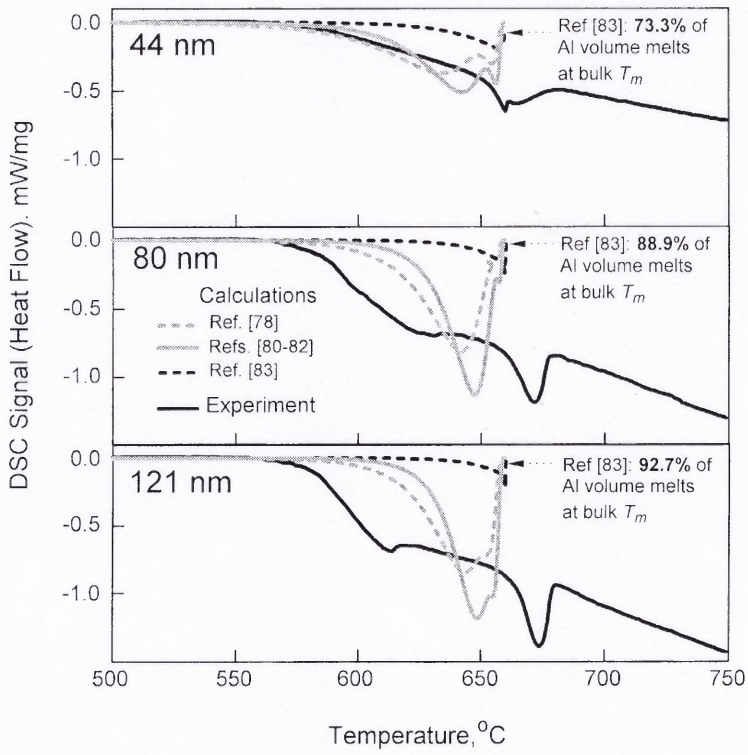

Figure 4.5 Experimental and computed DSC curves showing melting of aluminum nanopowders.

It was found that the shapes of the predicted curves are very sensitive to the specific type of the particle size distribution, e.g., bimodal vs. single mode lognormal distribution. The melting curves can further depend on the specific surface morphologies of the used nanoparticles that could affect the sizes of melting nano-domains.

4.6 Conclusion

Melting and oxidation of aluminum nanopowders are studied experimentally and the results are compared with the predictions of several models published to date. Experiments showed that the oxidation and melting onsets of the heated aluminum nanopowders do not correlate, consistently with the conclusion made earlier for the micron-sized aluminum powders. The melting of nanopowders starts at a lower temperature than the melting point of bulk aluminum; however, existing models describe the effect of the particle size on the melting point depression only qualitatively. Detailed analysis of the particle size distributions and surface morphology is needed for further quantitative verification of any related models. A recent oxidation mechanism taking into account polymorphic phase changes in the Al_2O_3 layer describes oxidation of the nanopowders satisfactorily. The particle-size dependent oxidation model developed in the study was successful in describing the experimental TGA curves. The same model was used to evaluate the particle size dependent thickness of the oxide layer produced on the aluminum nanopowders during their storage at room temperature. Observed minor inconsistencies between predictions of the proposed oxidation model and TGA measurements can be related to the extreme sensitivity of the oxidation rates to the

specific shape of the particle size distribution that was described in this work by a superposition of two lognormal functions.

CHAPTER 5

CONCLUSIONS

The study started from a literature review of data on aluminum ignition temperatures and available ignition models. The review clearly demonstrated a dependence of the reported aluminum ignition temperatures on the size of samples used in experiments. It was also identified that the existing models propose different mechanisms for ignition of nanosized and coarse powders igniting at low and high temperatures, respectively. At the same time, no consistent ignition mechanisms were proposed for the 1- 50 μm powders, which are most widely used in practical applications, and which were observed to ignite in a broad range of temperatures.

In this study, a new model was developed that enables one to describe quantitatively ignition of aluminum powders of different sizes using a common formulation and a consistent approach. Ignition is caused by the heterogeneous exothermic processes occurring within the oxide film on the Al particle surface. The model considers polymorphic phase transformations within the aluminum oxide layer and describes diffusion of various species through the alumina film. The polymorphic phase transitions occurring in Al_2O_3 upon its heating and growth are accompanied by changes in its density and crystallinity, which affect the continuity and diffusion resistance of the protective alumina layers. These changes account for the observed step-wise changes in the oxidation rate. The kinetics of different heterogeneous processes resulting in aluminum ignition in oxygenated environments were determined experimentally from thermal analysis. The model successfully explains a wide range of ignition temperatures

reported in the literature and the dependence of ignition temperatures on the size of aluminum particles.

Additional studies should be undertaken to take advantage of the proposed model of aluminum ignition for practical applications of using aluminum combustion in energetic formulations. The experiments with simple and readily described heat transfer configurations are especially useful to elucidate the effects of different polymorphic transformations and oxidation processes on ignition. For example, experiments with well controlled environments and shock-wave ignition of aluminum particles with narrow size distributions are suggested. The heat transfer model for these experiments is straightforward and the environment temperatures can be readily controlled. In addition, experiments with varied and well controlled heating rates and monodisperse aluminum powders are also desirable to verify the specific effects of oxidation and phase transformation kinetics. Finally, effects of different oxidizing environments on the kinetics of heterogeneous processes that control ignition are expected to be significant. Specifically, heterogeneous oxidation kinetics of aluminum in carbon dioxide and water vapor should be determined experimentally and incorporated into the ignition model.

APPENDIX

DETERMINATION OF OXIDE THICKNESS FROM TGA DATA

The experimental mass change of an oxidized aluminum sample was converted into the change of thickness of the alumina surface layer. Based on the x-ray diffraction analysis of partially oxidized powders, it was established that the oxide layer was amorphous during stage 1 oxidation; the majority of oxide was γ-alumina during stage 3, and oxide converted to α-alumina during stage 4 [13]. Different oxide polymorphs have different densities and therefore, in Fig. 3.3, the experimental oxide thickness history is represented by three lines, corresponding to the separate evolution of amorphous, γ- and α-alumina, respectively (see description of Fig. 3.3 in the chapter 3). The lines overlap in the temperatures ranges were phase transformations occur. The distance between lines in the regions where they overlap provides an estimate of accuracy which can be expected from the calculations of the oxide thickness.

It is assumed that aluminum powder is initially covered by a natural amorphous oxide film. The initial external radius of the film, r'_{am} , equals that obtained from the BET measurements: $r'_{am} = r_{BET}$. The radius of the metallic aluminum is obtained as: $r'_{Al} = r'_{am} - h'_{am}$, where the initial layer thickness h'_{am} is assumed to be 2.5 nm [50-52, 66], significantly smaller than the particle radius: $h'_{am} << r'_{am}$.

Evaporation of aluminum and its oxidation products are neglected. Therefore, the mass of aluminum within a particle is conserved. For spherical particles and assuming

(only to determine the oxide thickness history) that at any moment only one type of oxide is covering a particle, that conservation can be expressed as:

$$\rho_{Al} r_{Al}'^3 + \frac{2\mu_{Al}}{\mu_{Al_2O_3}} \rho_{am} (r_{am}'^3 - r_{Al}'^3) = \rho_{Al} r_{Al}^3 + \frac{2\mu_{Al}}{\mu_{Al_2O_3}} \rho_{ox} (r_{ox}^3 - r_{Al}^3) \qquad \text{(A1)}$$

where μ_{Al} and $\mu_{Al_2O_3}$ are the molar masses of aluminum and aluminum oxide, correspondingly.

In the TGA experiments, the measured mass always slightly decreased when the sample was heated from room temperature to about 300 °C. This effect was most likely caused by the removal of adsorbed moisture. The minimal mass of the sample measured during its heating (at about 300 °C) was considered as the initial sample mass, m_S' for interpretation of TGA. The normalized sample mass, m_N, is expressed as the ratio of the mass of oxidized powder, m_S, to its initial mass:

$$\frac{m_S}{m_S'} = m_N . \qquad \text{(A2)}$$

For monodispersed, spherical particles, equation (A3) can be rewritten as:

$$\frac{\rho_{Al} r_{Al}^3 + \rho_{ox} (r_{ox}^3 - r_{Al}^3)}{\rho_{Al} r_{Al}'^3 + \rho_{am} (r_{am}'^3 - r_{Al}'^3)} = m_N . \qquad \text{(A3)}$$

There are only two unknown parameters, r_{ox} and r_{Al}, in the system of equations (A1; A3) The solution for r_{Al} is:

$$r_{Al} = f_1(m_N) = U \left[1 - \frac{2\mu_{Al} J}{\mu_{Al_2O_3}} \right]^{1/3} \qquad \text{(A4)}$$

where

$$U = \left[r_{Al}'^3 + \frac{2\mu_{Al}}{\mu_{Al_2O_3}} \frac{\rho_{am}}{\rho_{Al}} (r_{am}'^3 - r_{Al}'^3) \right]^{1/3} \tag{A5}$$

and

$$J = \frac{m_N}{U^3} \left[r_{Al}'^3 + \frac{\rho_{am}}{\rho_{Al}} (r_{am}'^3 - r_{Al}'^3) \right]. \tag{A6}$$

For the external radius of the oxide layer, the solution is:

$$r_{ox} = f_2(m_N) = \left[U^3 \frac{\rho_{Al}}{\rho_{ox}} \frac{J-1}{1 - \frac{2\mu_{Al}}{\mu_{Al_2O_3}}} + r_{Al}^3 \right]^{1/3}. \tag{A7}$$

Finally, the oxide thickness, h_{ox}, is the difference between r_{ox} determined from equation (A7) and r_{Al} obtained from equation (A4).

REFERENCES

1. Price, E.W., Sigman, R.K. (2000). Combustion of Aluminized Solid Propellants. Progress in Astronautics and Aeronautics, 185, Solid Propellant Chemistry, Combustion, and Motor Interior Ballistics, ed. V. Yang, T. Brill, & W. Ren, American Institute of Aeronautics and Astronautics, 663-688.

2. Dong, H., Zhumei, S. (1996). Study of the Fast Reaction Characteristics of Aluminized PETN Explosive Powders. Combustion and Flame, 105 (3), 428-430.

3. Hickman, S.R., Brewster, M.Q. (1996). Oscillatory Combustion of Aluminized Composite Propellants. Twenty-Sixth's Symposium (International) on Combustion Volume 2, 2007-2015.

4. Babuk, V.A, Vasilyev, V.A. (2002). Model of Aluminum Agglomerate Evolution in Combustion Products of Solid Rocket Propellant. Journal of Propulsion and Power, 18 (4), 814-823.

5. Friedman, R., Macek, A. (1962). Ignition and Combustion of Aluminum Particles in Hot Ambient Gases. Combustion and Flame, 6, 9-19.

6. Brossard, C., Ulas, A., Yen, C.L., & Kuo, K.K. (1997). Ignition and Combustion of Isolated Aluminum Particles in the Post-Flame Region of a Flat-Flame Burner. 16th International Colloquium on the Dynamic of Explosions and Reactive Systems (Krakow, Poland, Aug 3-8,1997).

7. Brzustowski, T. A., Glassman, I. (1964). Vapor-Phase Diffusion Flames in the Combustion of Magnesium and Aluminum - Part II Experimental Observations in the Oxygen Atmospheres. Progress in Astronautics and Aeronautics, 117-158.

8. Kuehl, D.K. (1965). Ignition and Combustion of Aluminum and Beryllium. AIAA Journal, 3 (12), 2239-2247.

9. Merzhanov, A.G., Grigorjev, Yu. M., & Galchenko, Yu. A. (1977). Aluminum Ignition. Combustion and Flame, 29, 1-14.

10. Yuasa, S., Zhu, Y., & Sogo, S. (1997). Ignition and Combustion of Aluminum in Oxygen/Nitrogen Mixture Streams, Effects of Oxygen Concentration on Combustion of Aluminum in Oxygen/Nitrogen Mixture Streams, Combustion and Flame, 108, 387-396.

11. Johnson, C., Parr, T., Hanson-Parr, D., Hollins, R., Fallis, S., & Higa, K. (2000). Combustion and Oxidation of Metal Nanoparticles and Composite Particles, Proceedings of 37-th JANNAF Combustion Subcommittee Meeting (November 2000), 539-555.

12. Bulian, C.J., Kerr, T.T., & Puszynski, J.A. (2004). Ignition Studies of Aluminum and Metal Oxide Nanopowders. Proceedings of the Thirty-First International Pyrotechnics Seminar, Schelling, F.J. - Editor, IPSUSA Seminars, Inc., Fort Collins, CO, 327-338.

13. Trunov, M.A., Schoenitz, M., & Dreizin, E.L. (2005). Effect of Polymorphic Phase Transformations in Al_2O_3 Film on Oxidation Kinetics of Aluminum Powders. Combustion and Flame, 140, 310-318.

14. Zhu, Y., Yuasa, Y. (1998). Effects of Oxygen Concentration on Combustion of Aluminum in Oxygen/Nitrogen Mixture Streams. Combustion and Flame, 115 (3), 327-334.

15. Assovskiy, I.G., Zhigalina, O.M., & Kolesnikov-Svinarev, V.I. (1999) Gravity Effect in Aluminum Droplet Ignition and Combustion, in: Fifth International Microgravity Combustion Workshop (Cleveland, USA, May 18-20, 1999), NASA, 223-226.

16. Alekseev, A.G., Barlas, R.A., Tsidelko, T.I., & Shapoval A.F. (1971). Effect of Particle Size on the Combustibility and Explosion Parameters of Dispersed Aluminum and Magnesium Powders. in: Nedin, V.V. (Ed.), Preduprezhdenie Vnezapnykh Vzryvov Gazodispersnykh Sistem, 66-73 (in Russian).

17. Belyaev, A.F., Frolov, Yu.V., & Korotkov, A.I. (1968) Combustion and Ignition of Particles of Finely Dispersed Aluminum, Fizika Goreniia i Vzryva, 4 (3), 323-329 (in Russian).

18. Derevyga, M.E., Stesik, L.N., & Fedorin, E.A. (1977). Study of the Ignition and Combustion of Aluminum and Zinc in Air. Combustion, Explosion, and Shock Waves, 13 (6), 722-726.

19. Ermakov, V.A., Razdobreev, A.A., Skorik, A.I., Pozdeev, V.V., & Smolyakov, S.S. (1982). Temperature of Aluminum Particles at the Moments of Ignition and Combustion. Fizika Goreniya i Vzryva, 18 (2), 141-143 (in Russian).

20. Fedoseev, V.A. (1970). Combustion of Magnesium and Aluminum Particles in Different Media, Fizika Aerodispersnykh Sistem, 3, 61-72 (in Russian).

21. Henry, B.M., Dinelli, F., Zhao, K.-Y., Grovenor, C.R.M., Kolosov, O.V., Briggs, G.A.D., Roberts, A.P., Kumar, R.S., & Howson R.P. (1999). Microstructural Study of Transparent Metal Oxide Gas Barrier Films. Thin Solid Films, 355(1), 500-505.

22. Brooks, K.P., Beckstead M.W. (1995). Dynamics of Aluminum Combustion, AIAA Journal of Propulsion and Power, 11, 769-780.

23. Boiko, V.M., Poplavski, S.V. (2002). Self-Ignition and Ignition of Aluminum Powders in Shock Waves, Shock Waves, 11 (4), 289-295.

24. Benkiewicz, K., Hayashi, A.K. (2002). Aluminum Dust Ignition Behind Reflected Shock Wave: Two-Dimensional Simulations. Fluid Dynamics Research, 30, 269-292.

25. Rozenband, V.I., Vaganova, N.I. (1992). A Strength Model of Heterogeneous Ignition of Metal Particles, Combustion and Flame, 88 (1), 113-118.

26. Rozenband, V.I. (2004). Thermo-Mechanical Aspects of The Heterogeneous Ignition of Metals, Combustion and Flame, 137, 366-375.

27. Schaller, R. (2000). Mechanical Spectroscopy of the High-Temperature Brittle-to-Ductile Transition in Ceramics and Cermets, Journal of Alloys and Compounds, 310, 7-15.

28. Fedorov, A.V., Kharlamova, Y.V. (2003). Ignition of an Aluminum Particle. Combustion, Explosion, and Shock Waves, 39, 544-547.

29. Rode, H., Hlavacek, V., Viljoen, H.J., & Gatica, J.E. (1992). Combustion of Metallic Powders: A Phenomenological Model for Initiation of Combustion, Combustion Science and Technology, 88, 153-175.

30. George, P., DesJardin, P.E. (2003). Towards a Mechanistic Model for Aluminum Particle Combustion. ASME Proceedings of Summer heat Transfer Conference, HT2003-47499, (Las Vegas, Nevada, 20-23 July, 2003), 161-168.

31. Kubaschewski, O., Hopkins, B.E. (1962). Oxidation of Metals and Alloys, London: Butterworths & Co., 319.

32. Medvedev, A.E., Fedorov, A.V., & Fomin V.M. (1982). Mathematical Modeling of Metal Particle Ignition in the High-Temperature Flow Behind a Shock. Combustion, Explosions, and Shock Waves, 18(3), 261-264.

33. Alekseeva, T.I., Gurevich, M.A., & Ozerov, E.S. (1967). Combustion of Aluminum Particles. Trudy - Leningradskii Politekhnicheskii Institut imeni M. I. Kalinina, 280, 98-106 (in Russian).

34. Gurevich, M.A., Lapkina, K.I., & Ozerov, E.S. (1970). Limiting Conditions of Aluminum Particle Ignition. Fizika Goreniya i Vzryva, 6(2), 172-176 (in Russian).

35. Tao H. (2002). Shock Wave Ignition of Aluminum Particles. Journal of Physics IV France, 12, Pr7-105 - Pr-112.

36. Roberts, T.A., Burton, R.L., & Krier, H. (1993) Ignition and Combustion of Aluminum/Magnesium Alloy Particles in O_2 at High Pressures. Combustion and Flame, 92, 125-143.

37. Kiselev, V.I., Leipinskikh, B.M. (1974). Kinetics of Oxidation of Molten Aluminum. Institute of Metallurgy, Sverdlovsk, USSR, VINITI 542-74, 1-12 (in Russian).

38. Elytin, V.P., Mitin, B.S., & Samotekin, V.V. (1971). Effect of Oxygen Pressure on the Oxidation of Aluminum. Izvestiya Akademii Nauk SSSR, Metally, 3, 227-230 (in Russian).

39. Tompa, A.S., Boswell, R.F., Skahan, P., & Gotzmer, C. (1997). Low/High Temperature Relationships in Dinitramide Salts by DEA/DSC and Study of Oxidation of Aluminum Powders by DSC/TG, Journal of Thermo Analysis, 49 (3), 1161-1170.

40. Mitin, B. S., Samoteikin. V.V. (1971). Oxidation of Molten Aluminum. Zhurnal Fizicheskoi Khimii, 45(3), 730-734 (in Russian).

41. Bergsmark, E., Simensen, C.J., & Kofstad, P. (1989). The Oxidation of Molten Aluminum. Materials Science and Engineering, A120, 91-95.

42. Price, E.W. (1984). Combustion of Metalized Propellants. Progress in Astronautics and Aeronautics, 90, 479-513.

43. Dreizin, E.L. (1996). Experimental Study of Stages in Aluminum Particle Combustion in Air. Combustion and Flame, 105, 541-556.

44. Levin, I., Brandon, D. (1998). Metastable Alumina Polymorphs: Crystal Structures and Transitions Sequences. Journal of American Ceramic Society, 81(8), 1995-2012.

45. Jeurgens, L.P.H., Sloof, W.G., Tichelaar, F.D., & Mittemeijer, E.J. (2000). Thermodynamic Stability of Amorphous Oxide Films on Metals: Application to Aluminum Oxide Films on Aluminum Substrates. Physical Review B, 62 (7), 4707-4719.

46. Jeurgens, L.P.H., Sloof, W.G., Tichelaar, F.D., & Mittemeijer, E.J. (2002a). Structure and Morphology of Aluminum-Oxide Films Formed by Thermal Oxidation of Aluminum. Thin Solid Films, 418, 89-101.

47. Jeurgens, L.P.H., Sloof, W.G., Tichelaar, F.D., & Mittemeijer, E.J. (2002b). Growth Kinetics and Mechanisms of Aluminum Oxide Films Formed by Thermal Oxidation of Aluminum. Journal of Applied Physics, 92 (3), 1649-1656.

48. Riano, O.A., Wadsworth, J., & Sherby, O.D. (2003). Deformation of Fine-Grained Alumina by Grain Boundary Sliding Accommodated by Slip. Acta Materialia, 51, 3617-3634.

49. Sanchez-Lopez, C., Gonzalez-Elipe, A.R., & Fernandez, A. (1998). Passivation of Nanocrystalline Al Prepared by the Gas Phase Condensation Method: An X-Ray

Photoelectron Spectroscopy Study. Journal of Materials Research, 13 (3), 703-710.

50. Doherty, P.E., Davis, R.S. (1963). Direct Observation of the Oxidation of Aluminum Single-Crystal Surfaces. Journal of Applied Physics, 34, 619-628.

51. Tomas, K., Roberts, M.W. (1961). Direct Observation in the Electron Microscope of Oxide Layers on Aluminum. Journal of Applied Physics, 32, 70-75.

52. Steinheil, A. (1934). The Structure and Growth of Thin Surface Films on Metals on Oxidation in Air, Annals of Physics, 19 (5), 465-483.

53. McHale, J.M., Auroux, A., Perrotta, A.J., & Navrotsky, A. (1977) Surface Energies and Thermodynamic Phase Stability in Nanocrystalline Aluminas. Science, 277, 788-791.

54. Kwon, Y.-S., Gromov, A.R., & Ilyin, A.P. (2002). Reactivity of Superfine Aluminum Powders Stabilized by Aluminum Diboride. Combustion and Flame, 131 (3), 349-352.

55. Il'in, A.P., Gromov, A.A., & Yablunovskii, G.V. (2001). Reactivity of Aluminum Powders. Combustion, Explosion, and Shock Waves, 37 (4), 418-422.

56. Jones, D.E.G., Brousseau, P., Fouchard, R.C., Turcotte, A.M., & Kwok, Q.S.M. (2000). Thermal Characterization of Passivated Nanometer Size Aluminum Powders. Journal of Thermal Analysis and Calorimetry, 61, 805-818.

57. Mench, M.M., Kuo, K.K., Yeh, C.L., & Lu, Y.C. (1988). Comparison of Thermal Behavior of Regular and Ultra-Fine Aluminum Powders (Alex) Made From Plasma Explosion Process. Combustion Science and Technology, 135 (1-6), 269-292.

58. Pivkina, A., Frolov, Y., Zavyalov, S., Ivanov, D., Schoonman, J., Streletskii, A., & Butyagin, P. (2004). Ultra-Fine and Nanosized Oxidizers and Metals: Thermal Properties and Use in High Energetic Compositions. Proceedings of the Thirty-First International Pyrotechnics Seminar, Schelling, F.J. (Ed.), IPSUSA Seminars, Inc., Fort Collins, CO, 285-298.

59. Eisenreich, N., Fietzek, H., Juez-Lorenzo, M.M., Kolarik, V., Koleczko, A., & Weiser, V. (2004). On the Mechanism of Low-Temperature Oxidation for Aluminum Particles Down to Nano-Scale, Propellants, Explosives, Pyrotechnics, 29 (3), 137-145.

60. Trunov, M.A., Schoenitz, M., & Dreizin, E.L. (2005). Ignition of Aluminum Powders Under Different Experimental Conditions. Propellants, Explosives, Pyrotechnics, 30, 36-43.

61. Trunov, M.A., Schoenitz, M., & Dreizin, E.L. (2006). Effect of Polymorphic Phase Transformations in Alumina Layer on Ignition of Aluminum Particles. Combustion Theory and Modeling, [in print].

62. Kissinger, HE. (1957). Reaction Kinetics in Differential Thermal Analysis. Analytical Chemistry, 29, 1702-1706.

63. Mittemeijer, E.J. (1992). Analysis of the Kinetics of Phase Transformations. Journal of Materials Science, 27, 3977-3987.

64. Simpson, T.W., Wen, Q., Yu, N., & Clarke, D.R. (1998). Kinetics of the Amorphous $\rightarrow\gamma\rightarrow\alpha$ Transformations in Aluminum Oxide: Effect of Crystallographic Orientation. Journal of American Ceramic Society, 81, 61-66.

65. Dorre, E, Hubner, H. (1984). Alumina: Processing, Properties and Applications. Berlin: Springer-Verlag.

66. Ramaswamy, A.L., Kaste, P., & Trevino, S.F. (2004). A "Micro-Vision" of the Physio-Chemical Phenomena Occurring in Nanoparticles of Aluminum. Energetic Materials, 12, 1-24.

67. Dwivedi, R.K., Gowda, G. (1985). Thermal Stability of Aluminum Oxides Prepared from Gel. Journal of Materials Science Letters, 4, 331-343.

68. Yen, F.S., Chang, J.L., & Yu, P.C. (2003). Growth Thermodynamics and Kinetics of Nano-Sized Alpha-Al_2O_3 Powders. Key Engineering Materials, 249, 179-182.

69. Ulhmann, D.R. (1972). A Kinetic Treatment of Glass Formation. Journal of Non-Cristyllite Solids, 7, 337-348.

70. Davis, H.A. (1976). The Formation of Metallic Glasses. Physics and Chemistry of Glasses, 17, 159-173.

71. Boiko, V.M., Lotov, V.V., & Papyrin, A.N. (1989). Ignition of Gas Suspension of Metallic Powders in Reflected Shock Waves. Combustion, Explosion, and Shock Waves, 25, 193-199.

72. Itano, Y., Hayashi, A.K., & Sato, H. (2003). Ignition and Combustion Characteristics of Solid Particles in High Temperature Region Behind a Reflected Shock Wave. Plasma Applications and Hybrid Functionality Materials, 12, 107-110.

73. Reynolds, P.M. (1961). Spectral Emissivity of 99.7% Aluminum Between 200 and 540°. British Journal of Applied Physics, 12, 111-114.

74. Shafirovich, E., Bocanegra, P.E., Chauveau, C., & Gökalp, I. (2004). Nanoaluminium - Water Slurry: A Novel "Green" Propellant for Space Applications. European Space Agency, (Special Publication) ESA SP, 557, 71-73.

75. Brousseau, P., Anderson, C.J. (2002). Nanometric Aluminum in Explosives. Propellants, Explosives, Pyrotechnics, 27 (5), 300-306.

76. Pivkina, A., Ulyanova, P., Frolov, Y., Zavyalov, S., & Schoonman, J. (2004). Nanomaterials for Heterogeneous Combustion. Propellants, Explosives, Pyrotechnics, 29 (1), 39-49.

77. Son, S.F. (2005). Materials Progress: Nanoaluminum, Metal Oxides Make Energetic Explosives. Advanced Materials and Processes, 163 (4), 11.

78. Reiss, H., Wilson, I.B. (1948). The Effect of Surface on Melting Point. Journal of Colloid Science, 3, 551-561.

79. Revesz, A. (2005). Melting Behavior and Origin of Strain in Ball-Milled Nanocrystalline Al Powders. Journal of Materials Science, 40, 1643-1646.

80. Jiang, Q., Yang, C.C., & Li, J.C. (2002). Melting Enthalpy Depression of Nanocrustals. Material Letters, 56, 1019-1021.

81. Liang, L.H., Li, J.C., & Jiang, Q. (2003). Size-Dependent Melting Depression and Lattice Contraction of Bi Nanocrystals. Physica B, 334, 49-53.

82. Zhao, M., Jiang, Q. (2004). Melting and Surface Melting of Low-Dimensional In Crystals. Solid State Communications, 130, 37-39.

83. Eckert, J., Holzer, J.C., Ahn, C.C., Fu, Z., & Johnson, W.L. (1993). Melting Behavior of Nanocrystalline Aluminum Powders. Nanostructured Materials, 2, 407-413.

84. Rai, A., Lee, D., Park, K., & Zachariah, M.R. (2004). Importance of Phase Change of Aluminum in Oxidation of Aluminum Nanoparticles. Journal of Physical Chemistry B, 108 (39), 14793-14795.

85. Granier, J.J., Pantoya, M.L. (2004). Laser Ignition of Nanocomposite Thermites. Combustion and Flame, 138, 373-383.

86. Wilson, D.E., Kim, K. (2003). A Simplified Model for the Combustion of Al/MoO_3 Nanocomposite Thermites. 39th AIAA/ASME/SAE/ASEE Joint Propulsion Conference, presentation AIAA-2003-4536.